

# Constraining the earthquake recording threshold of intraslab earthquakes with turbidites in southcentral Alaska's lakes and fjords

Drake M Singleton<sup>1</sup>, Daniel Brothers<sup>1</sup>, Peter J Haeussler<sup>1</sup>, Robert C Witter<sup>2</sup>, and Jenna C Hill<sup>2</sup>

<sup>1</sup>Affiliation not available

<sup>2</sup>United States Geological Survey

November 3, 2023

## Abstract

Intraslab earthquakes do not produce primary paleoseismic evidence at the Earth's surface, making efforts to develop an event chronology challenging. However, the strong ground motion from intraslab events may initiate gravity-driven turbidity flows in subaqueous basins; the resulting deposits (turbidites) can provide a paleoseismic proxy if the conditions that initiate these flows are known. To better constrain the initiating conditions, we use two recent intraslab earthquakes in southcentral Alaska, the Mw 7.1 November 30, 2018, Anchorage and the Mw 7.1 January 24, 2016, Iniskin earthquakes, as calibration events. Through a multi-lake investigation spanning a range of shaking intensities and based on a combined geological and geophysical dataset, we document the occurrence, or absence, of earthquake-generated turbidity flows from these two earthquakes. The 2018 and 2016 earthquakes are recorded by centimeter-scale turbidites that can be differentiated from climatically generated deposits, as well as other seismic sources (i.e., the 1964 Alaska megathrust earthquake) based on deposit thickness, sedimentological properties, and deposit age. We show that a Modified Mercalli Intensity (MMI) of  $\sim V-V1/2$  is the minimum shaking intensity required to generate localized sediment remobilization from deltaic slopes, and a MMI of  $\sim V1/2$  is required to produce a deposit of sufficient thickness that a seismic origin can be confidently assigned. Deltaic slopes are the major source of remobilized sediment that record the 2018 and 2016 events, however sediment from non-tributary sourced basin slopes may become remobilized in steep-sloped, high sedimentation areas, and under elevated shaking intensity. The documentation of seismically generated deposits in quick succession ( $\sim 2$  years) with diagnostic features that can be assigned to the seismic source highlights the utility of using recent earthquakes as calibration events to investigate the subaqueous response to strong ground motion.

## 1. Introduction

Over the past two decades a series of intraslab earthquakes along the west coast of North America have caused significant damage to infrastructure and on occasion fatalities (Chang and Falit-Baiamonte, 2002; Sahakian, et al., 2018; West et al., 2020). Quantifying the recurrence intervals and spatial distribution of intraslab earthquakes, which are earthquakes that occur within the subducting oceanic plate, currently relies on frequency-magnitude relationships from instrumented records and historically documented events that are limited to the last  $\sim 130$  years. Reconstructing longer geologic records of intraslab earthquakes with traditional paleoseismic methods is challenging. Unlike megathrust and crustal faults, faults within subducting slabs do not produce primary coseismic deformation at the Earth's surface (e.g., surface fault rupture or significant land-level change). The lack of primary evidence for intraslab earthquakes results in a spatial and rate-smoothed representation in probabilistic seismic hazard assessments (Frankel et al., 2015) that may not fully capture the associated hazard, as the input parameters, including the spatial extent of, and recurrence interval for, strong ground motion remain poorly understood (West et al., 2020). Thus,

alternative approaches are needed to reconstruct histories of strong ground motions from intraslab events, which can then be incorporated into seismic hazard analysis.

Paleoseismic archives may be found in lake and fjord basins with sedimentary environments that form and preserve evidence of strong ground motions. Indicators of strong ground motions often include coseismically triggered mass transport deposits (MTDs) (Strasser et al., 2006; Haeussler et al., 2014; Brothers et al., 2016; Praet et al., 2017; Roland et al., 2020), soft sediment deformation (Heifetz et al., 2005; Avşar et al., 2016; Molenaar et al., 2022), and geochemical signatures in basin deposits (Avşar et al., 2014a; 2014b). However, as with deep-sea marine paleoseismic investigations (e.g., Goldfinger et al., 2012; Patton et al., 2013; Howarth et al., 2021), most studies in lacustrine and fjord settings use turbidites to reconstruct records of strong ground motion (e.g., Beck, 2009; Moernaut, et al., 2014; Van Daele et al., 2015; Praet et al., 2017; Vandekerckhove et al., 2020; Van Daele et al., 2020; Wils et al., 2021; Praet et al., 2022).

Vital to interpreting an earthquake record from lakes and fjords is an understanding of the sensitivity of subaqueous basins to strong ground motion. The Earthquake Recording Threshold (EQRT) is the minimum shaking intensity required to trigger a sediment-gravity flow that produces a deposit of sufficient thickness and character to be distinguished from background deposits within a specific basin (Moernaut et al., 2014; Van Daele et al., 2015). Several studies have shown that shaking during intraslab earthquakes is strong enough to generate turbidity currents in lakes and fjords (e.g., Moernaut, et al., 2014; Van Daele et al., 2019; 2020; Praet et al., 2022). The initial studies on EQRT in lakes along the Chilean subduction zone found that for sediment to be remobilized on deltaic slopes ground motion must reach a value of at least Modified Mercalli Intensity (MMI)  $\sim V1/2-V3/4$ , while a slightly higher shaking intensity is needed for non-tributary sourced (basin) slopes (Moernaut et al., 2014; Van Daele et al., 2015). The EQRT is dependent on several factors including catchment steepness and vegetation, basin physiography, and sedimentological properties. Because different tectonic and sedimentological settings can result in variations in the EQRT for a particular basin (Van Daele et al., 2015), the EQRT for one region may not be applicable to another, and it is necessary to calibrate a regional EQRT with historical events before investigating the pre-historic record.

In this paper, we use two well-documented intraslab earthquakes, the  $M_w$  7.1 2018 Anchorage and the  $M_w$  7.1 2016 Iniskin earthquakes, as calibration events to investigate the geological sensitivity of several lakes and fjords in southcentral Alaska to strong ground motion. The 2016 Iniskin and 2018 Anchorage earthquakes are particularly advantageous events for this purpose because both earthquakes are well-recorded (Mann and Abers, 2020; West et al., 2020; USGS, 2016a; 2018) with identical magnitudes and epicenters at opposite ends of the Cook Inlet that produced shaking intensities with opposite gradients across the study area (Figure 1). We present results from a multi-lake geophysical and coring effort that examines the spatial distribution, sedimentological characteristics, and remobilized sediment sources of turbidites that record the 2016 or 2018 earthquakes. We use these results to constrain the EQRT in southcentral Alaska and to investigate deposit variations in response to different shaking intensities.

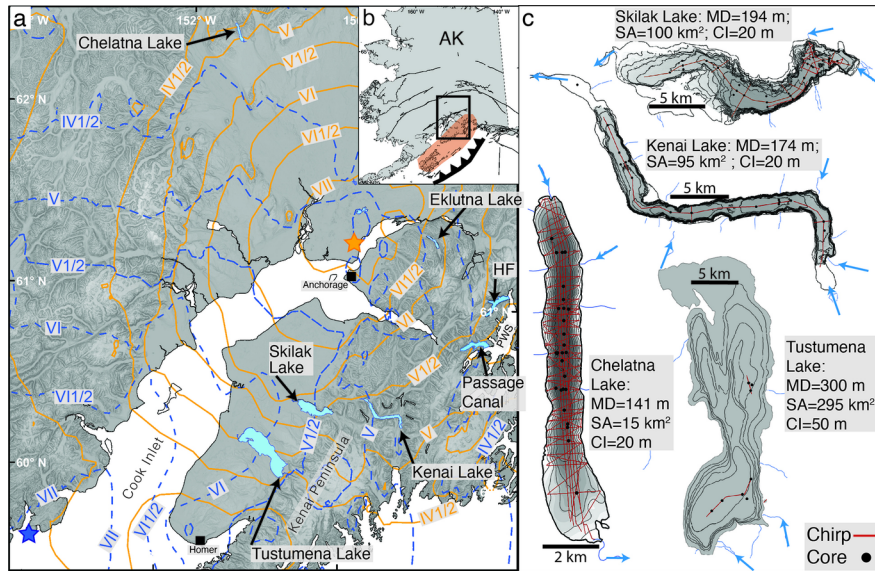


Figure 1: (a) Map of the Cook Inlet region. Solid gold lines and star represent the 2018 Anchorage earthquake MMI contours and epicenter (USGS, 2018). Dashed blue lines and star represents the 2016 Iniskin earthquake MMI contours and epicenter (USGS, 2016a). HF=Harriman Fjord; PWS=Prince William Sound (b) Inset shows map of Alaska with main plate boundary (toothed) and crustal faults (thin lines) (USGS, 2020). The rupture area of the 1964 M 9.2 earthquake corresponds to the shaded red region (Plafker, 1969). Black box denotes approximate location of study region shown in part a. (c) Bathymetry of the surveyed lakes with main fluvial inputs and outlets (blue arrows). MD=Max Depth, SA=Surface Area, CI=Contour Interval. Bathymetry data from Haeussler et al., (2022) and ADFG, (2015).

## 2. Background

### 2.1 Calibration events: Historical earthquakes in southcentral Alaska

Subduction of the Pacific plate beneath the North American plate at a rate of  $\sim 57$  mm/yr (Altamimi et al., 2016) occurs along the Alaska-Aleutian megathrust that extends over 3700 km from Prince William Sound (PWS) in the east to the western end of the Aleutian Islands. On March 27, 1964, the eastern portion of the Alaska-Aleutian megathrust generated a  $M_w$  9.2 subduction earthquake—the second largest instrumentally recorded earthquake (USGS, 2016b). The earthquake hypocenter was located beneath PWS and fault rupture propagated southwestward for more than 650 km across the PWS, Kenai, and Kodiak sections (Plafker, 1969). Ground motion during the 1964 event was most intense above the area of coseismic displacement along the plate interface, an area that includes the Kenai Peninsula and several lakes investigated in this study (Figure 1), where estimated MMI was at least VII1/2 (Plafker, 1969; USGS, 2016b). Shaking induced submarine slope failures in fjords of PWS generated local tsunamis that impacted the coastal communities of Whittier, Seward, Valdez, and Chenega (Plafker et al., 1969; Haeussler et al., 2014; Brothers et al., 2016; Roland et al., 2020). Subaqueous slope failures and tsunamis also struck communities along lake shorelines on the Kenai Peninsula (McCulloch, 1966).

The  $M_w$  7.1 Iniskin earthquake on January 24, 2016, resulted from fault rupture in the subducting Pacific plate at a depth of 111 km (Mann and Abers, 2020). The epicenter is located  $\sim 106$  km due west of Homer, Alaska, and  $\sim 263$  km southwest of Anchorage (Figure 1). At the time, the 2016 earthquake was the largest instrumentally recorded intermediate-depth earthquake to occur in the Cook Inlet region (Mann and Abers, 2020). Anomalously high ground motions ( $>0.2$  g) in the Kenai Peninsula and Anchorage regions, relative to model predictions, suggest that along-slab path effects may have amplified strong ground motion in these areas (Mann and Abers, 2020).

The November 30, 2018,  $M_w$  7.1 Anchorage earthquake resulted from intraslab faulting at a depth of 47 km, with an epicenter  $\sim$ 14.5 km northwest of Anchorage (Figure 1) (West et al., 2020). In contrast to the 2016 Iniskin event, the shallowness of the hypocenter confined seismic waves to the upper-plate crust (Mann and Abers, 2020). The strongest shaking lasted 20-40 s in the Anchorage region with peak ground accelerations greater than 0.25 g observed over an  $\sim$ 8000 km<sup>2</sup> area (West et al., 2020). Although relatively short in duration ( $\sim$ 20-40 s), the distribution of shaking intensity was variable across the region with stations over 200 km from the epicenter recording acceleration values that spanned an order of magnitude (West et al., 2020).

## 2.2 Lacustrine Paleoseismology in southcentral Alaska and Study Sites

In this study, we examined four lakes in the upper Cook Inlet region (Skilak, Kenai, Tustumena, and Chelatna) and two fjords in western Prince William Sound (Passage Canal and Harriman Fjord) for sedimentary evidence of strong ground motion (Figure 1). Site selection was based in part on findings from prior subaqueous paleoseismology studies in southcentral Alaska, which we summarize below, along with the physiography of the targeted basins.

### 2.2.1. Eklutna Lake

Several recent studies document a paleoseismic record of earthquake shaking at Eklutna Lake, located 48 km east of the 2018 epicenter (Figure 1). Praet et al. (2017) mapped sublacustrine landslides (14 events total) in seismic reflection data that occur at the base of slope around both sub-basins within Eklutna Lake. Individual landslide-related seismic horizons are correlative across both proximal and distal basins, suggesting a seismic trigger (synchronicity criterion) (Schnellmann et al., 2002; Praet et al., 2017). Radionuclide dating indicates that the most recent landslide deposits are from the 1964 earthquake (MMI  $\sim$ VIII/2), which is expressed as a turbidite in sediment cores from the middle of the basin with a thickness between 0.9–55 mm (Praet et al., 2017; Boes et al., 2018; Vandekerckhove et al., 2020).

During the 2018 Anchorage earthquake, Eklutna Lake experienced MMI values of  $\sim$ VI-VII/2 (Figure 1) (USGS, 2018). In the hours following the earthquake, a ‘dirt streak’ (suspended sediment) was observed on the lake surface and turbidity values spiked at the Eklutna water facility’s intake pipe (Van Daele et al., 2020). In February 2019, Van Daele et al. (2020) collected 32 gravity cores (48–84 cm-long) that show a normally-graded turbidite at the top of the cores, which ranges in thickness from 0.8 mm in the distal basin to 24.2 mm near the main fluvial input. The spatial extent and sedimentological characteristics of the 2018 turbidite are similar to those of the 1964 turbidite including a distinctively lighter color, relatively poor sorting, and high basal grain size statistics, and are markedly different from historical flood deposits (Van Daele et al., 2020).

### 2.2.2. Skilak Lake

Skilak Lake, located  $\sim$ 80 km southwest of Anchorage (Figure 1), receives glacial-fluvial sediment via the Skilak and Kenai Rivers (Figure 2). Varved sediment accumulates at 0.5 cm/yr (Praet et al., 2017) and consists of silty basal layers that form in the spring through autumn with overlying clay caps that accumulate in the winter (Boes et al., 2018). Seismic mapping identified seven distinct MTD complexes of likely seismic origin in Skilak Lake, the youngest of which records shaking during the 1964 earthquake (Praet et al., 2017; 2022). The 1964 earthquake generated MMI values of VIII/2 at Skilak Lake and triggered a megaturbidite in the central basin identified in sediment cores as a thick deposit ( $\sim$ 50+ cm) with a sandy base that grades to a clay cap (Praet et al., 2017; 2022). Skilak Lake experienced MMI values of about VI/2 during both the 2016 and 2018 earthquakes (USGS, 2016a; USGS, 2018), and presents an opportunity to examine the sedimentary response between two earthquakes with similar shaking intensities (Figure 2).

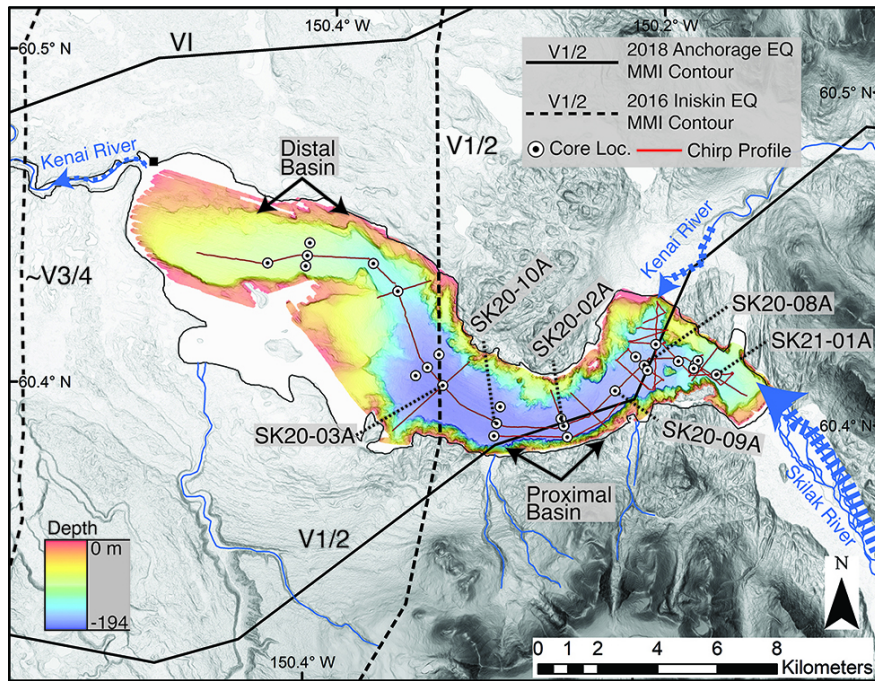


Figure 2: Bathymetric map of Skilak Lake with MMI contours (USGS, 2016a; 2018). The six labeled core locations correspond to grain size analysis in Figure 6a. Bathymetry data from Haeussler et al., (2022).

**Figure 2.** Bathymetric map of Skilak Lake with MMI contours (USGS, 2016a; 2018). The six labeled core locations correspond to grain size analysis in Figure 6a. Bathymetry data from Haeussler et al., (2022).

### 2.2.3. Kenai Lake

Kenai Lake occupies a narrow elongated glacial trough (2.5 km wide x 38 km long), that forms three semi-orthogonal segments that comprise distinct depositional basins (Figure 1). The sedimentation rate increases from  $\sim 0.25$  cm/yr in the western distal basin, to  $\sim 1$  cm/yr in the eastern part of the lake (Praet et al., 2017). Kenai Lake is varved, consisting of a coarse-grained (silt) spring to autumn base and a winter clay cap (Boes et al., 2018). Praet et al. (2017) identified seven distinct sublacustrine MTD complexes along with several associated megaturbidites in Kenai Lake. The most recent landslide complex and associated megaturbidite records the 1964 earthquake, which along with MMI values of  $\sim$ VIII $\frac{1}{2}$  caused a seiche and tsunami at Kenai Lake (McCulloch, 1966; Praet et al., 2017). Kenai Lake experienced MMI values of  $\sim$ V and  $\sim$ V $\frac{1}{4}$  during the 2016 and 2018 earthquakes, respectively (USGS, 2016a; USGS, 2018).

### 2.2.4. Tustumena and Chelatna Lakes

The next two study sites, Tustumena and Chelatna Lakes, are comparatively less well understood. Tustumena Lake is located  $\sim 110$  km southwest of Anchorage on the Kenai Peninsula and is a large, deep proglacial lake (Figure 1). Tustumena Lake experienced MMI values of  $\sim$ VIII $\frac{1}{2}$  in 1964 (USGS, 2016b),  $\sim$ VI during the 2016 Iniskin event, and  $\sim$ V during the 2018 Anchorage earthquake (USGS, 2016a; USGS, 2018). Chelatna Lake is located north of Cook Inlet and infills a glacial depression along the southern base of the Alaska Range (Figure 1). Chelatna Lake has a relatively small catchment area with glaciers covering about ten percent of the watershed. Chelatna Lake experienced MMI values of  $\sim$ V $\frac{1}{2}$  in 1964 (USGS, 2016b),  $\sim$ IV $\frac{1}{4}$  during the 2016 Iniskin event, and  $\sim$ V during the 2018 Anchorage earthquake (USGS, 2016a; USGS, 2018).

### 2.2.5. Passage Canal and Harriman Fjord

Passage Canal and Harriman Fjord are glacially fed fjords located within Prince William Sound (PWS)

~90 km southeast of Anchorage and directly above the 1964 megathrust rupture (Figure 1). Both fjords have a large, submerged moraine at the eastern fjord entrance, effectively forming an isolated basin similar in physiography to a proglacial lake. During the 1964 earthquake, Passage Canal and Harriman Fjord experienced MMI values of VIII/2 (USGS, 2016b), and a localized tsunami (32 m max run-up) in Passage Canal resulted from the collapse of the fjord head delta adjacent to the town of Whittier (Haeussler et al., 2014). During the 2016 and 2018 earthquakes, both fjord basins experienced MMI values of ~IV1/2 (2016) and ~V1/2 (2018) (USGS, 2016a; USGS, 2018).

### 2.3 Gravity driven turbidity flows generated by strong ground motions

The triggering of turbidity currents by strong ground motion is dependent on several factors related to submarine slope conditions and the intensity of shaking. Turbidity currents that develop from the disaggregation of large slope failures are dependent on the relationship between destabilizing forces (i.e., slope angle, sediment overburden, presence of weak layers, and ground motion or wave loading), and resisting forces related to the physical characteristics of the sediment (i.e., sediment cohesion and shear strength) (Piper and Normark, 2009; Strasser et al., 2006; Tailings, 2014; Moernaut et al., 2017). An alternative mechanism for the development of turbidity currents during strong ground motion is the remobilization of a thin veneer of surficial slope sediment that becomes mobile through the combined effects of (shaking induced) excess pore pressure and down-slope gravitational forces (Oguri et al., 2013; Moernaut et al., 2017; Molenaar et al., 2019; 2021).

In lakes and fjords, turbidity currents are typically triggered by either climatic forcing (e.g., intense flooding that develops into hyperpycnal flows) or strong ground motion from seismic waves (i.e., slope failure/MTDs and surficial sediment remobilization) (Beck, 2009; Talling, 2014; Haeussler et al., 2014; Brothers et al., 2016; Moernaut et al., 2017; Van Daele et al., 2017; Vandekerkhove et al., 2020). To first order, the subsequent turbidites generated by these different triggering mechanisms possess similar characteristics, such that differentiating between the causative sources can be complicated (e.g., Piper and Normark, 2009). At Eklutna Lake (Figure 1), Vandekerkhove et al. (2020) developed a series of diagnostic physical and sedimentological characteristics to differentiate between sediment-laden fluvial discharge lasting several hours to days versus rapid sediment remobilization by strong ground motion. Among the most reliable characteristics identified by Vandekerkhove et al. (2020) are the basal D80 value (defined in methods), a grain size statistic that is a proxy for the turbidity current's initial velocity and tends to be higher for earthquake-generated turbidites. Basal sorting was found to be generally poor for earthquake-generated turbidites due to the sudden onset followed by rapid waning of an earthquake-generated turbidity current (in contrast to flood conditions which may last several days) (Vandekerkhove et al., 2020). Additionally, earthquake turbidites tend to be lighter in color, a result of pigmentation loss in remobilized sediment and reduced organic component when compared to flood deposits (Vandekerkhove et al., 2020, Praet et al., 2022). Lastly, earthquake turbidites also exhibit ponding geometries such that the thickest deposits are found in the depositional center of the basin and rapidly thin towards the basin edges, a feature caused by the near-instantaneous initiation of turbidity currents deeper in the water column (below thermal/lake stratification) from multiple slopes by strong ground motion (Vandekerkhove et al., 2020). Given the similarities in catchment conditions with Eklutna Lake and the established large spatial extent of the 1964 deposit across southcentral Alaska (Haeussler et al., 2014; Brothers et al., 2016; Praet et al., 2017; Boes et al., 2018), these proxies will be useful in separating triggering mechanisms in the proglacial lakes and fjords examined in this study.

### 3. Methods

In summers 2020 and 2021, two field campaigns included an initial subbottom survey to image the subsurface geology and identify coring targets. Three Compressed High Intensity Radiated Pulse (Chirp) sub-bottom profiling systems were used in this study, each with theoretical vertical resolutions of less than ~10 cm. On the Kenai Peninsula lakes (i.e., Kenai, Skilak, and Tustumena Lakes) an Edgetech SB2400 operating with a frequency range of 4-24 kHz was deployed. An Edgetech SB3400 with a frequency range of 3-16 kHz was used to collect acoustic data on Chelatna Lake. Lastly, in Passage Canal an Edgetech SB2300-516 was deployed with a frequency range of 0.5-16 kHz. A seismic velocity of 1500 m/s is used in all time-to-depth conversions

and subsequent core-to-seismic correlations.

Percussion driven gravity cores (~2.5 m total liner length) were collected in a longitudinal profile along the basins, and several cross-basin transects targeted fluvial and fan deltas. On Kenai and Skilak Lakes, newly acquired cores were co-located at sites previously published, allowing for detailed comparisons and leveraging of published age models (Praet et al., 2017; Boes et al., 2018; Praet et al., 2022). Floral foam and sodium polyacrylate gel were used to stabilize the sediment-water interface upon recovery of each core. Cores were stored vertically from collection in the field until X-ray Computed Tomography scanning (CT-scans) was completed.

CT-scans of each core were acquired using a Geotek Rotating X-Ray (RXCT) scanner that operated at 115 kV and an effective tube current of 190 mA, which resulted in a resolution of 128 pixels per cm and a pixel size of 78 microns. X-ray radiodensities are expressed in CT-intensity and are dependent on the density and effective atomic number (chemical composition) of the sediment. Coarse sediment has a high radiodensity and appears bright in CT-scans, whereas clayey sediment has a low radiodensity and appears dark or dull in CT-scans. Turbidite thicknesses were measured in CT images with the ImageJ software package (Schneider et al., 2012), and for deposits with angular contacts, thicknesses were measured perpendicular to the contact. Errors in turbidite thickness are assigned the CT-scan resolution rounded up to the nearest tenth of a millimeter (i.e., 0.1 mm). Following CT-scanning, cores were logged at 1-cm intervals for physical properties (e.g., density, p-wave velocity, and loop sensor magnetic susceptibility (MS)). A selection of cores were split, photographed, described, and further measured with a Bartington MS Point Sensor at 2-mm intervals.

Event deposits, defined here as deposits with anomalous character relative to background sediments, are identified based mainly on thickness ( $> \sim 1$  cm) and grain size (coarser), and were sampled for grain-size analysis at 3-mm intervals. Samples were pretreated with hydrogen peroxide to remove organics and then disaggregated with sodium hexametaphosphate to reduced clay particle flocculation. Samples were then run through a Beckman Coulter LS 13-320 particle size analyzer with the Aqueous Liquid Module (ALM) and a measuring time of 60 secs after 10% sonification. Several grain-size statistics were calculated including D50, D80, and sorting values. The D50 (and D80) statistic is a measure of grain size fractionation and indicates the grain size diameter that 50 vol% (or 80 vol%) of the sample is smaller than.

On lakes without an established age model or datum, one core with continuous sedimentation and stratigraphic evidence of minimal erosion via turbidity currents was sampled for Cs-137 at 1-2 cm intervals. Radionuclide counts were done in a low-background, high-efficiency, well-shaped gamma ray detector with counts that were calibrated using certified reference materials (IAEA-300). Atmospheric testing of nuclear weapons between 1954 CE and 1963 CE resulted in significant production and fallout of radioactive isotopes peaking in 1963 CE, which are often well preserved in lacustrine sediments (Pennington et al., 1973). The 1964 earthquake triggered significant subaqueous slope failures across southcentral Alaska (Pflaker, 1969; Haeussler et al., 2014; Brothers et al., 2016; Praet et al., 2017), and its coincidence with the peak in Cs-137 makes it a reliable and widespread age datum.

Varve counting was performed on cores using CT-scans with the varve year boundary being identified as the winter clay cap, a ~0.3-3 mm-thick, low radiodensity unit in CT-scans (Boes et al., 2018). In lakes with an established age model and demonstrated varve formation, winter clay caps were counted back from the sediment-water interface starting with the collection year and checked against previous stratigraphic interpretations (Boes et al., 2012). For those basins without an established age model, we combined lamination counts and radionuclide dating to develop an age model.

Lastly, MMI values are estimated by interpolating the nearest U.S. Geological Survey (USGS) ShakeMap MMI contours to the basin edges and subsequently across the basin (USGS, 2016a; 2016b; 2016c; 2018). ShakeMap products were accessed several years after the 2016 and 2018 earthquakes allowing for additional model refinements to be incorporated into the MMI estimates. Therefore, values reported in this study may differ from earlier studies, specifically those related to the 2018 Anchorage earthquake (i.e., Van Daele et al., 2020). Reported MMI values given in the text for surveyed basins are the interpolated value in the middle

of the basin.

## 4. Results

### 4.1 Lacustrine Stratigraphy and Sedimentology

The lakes surveyed in this study are deep proglacial lakes and share several common physiographic characteristics. However, differences in catchment size, glacier proximity, basin morphology, and fluvial input result in variations in sediment character between lakes. Nevertheless, the general stratigraphy of the lakes surveyed consist of parallel high-amplitude reflections in Chirp data that thin and converge away from the main fluvial inputs. The background high-amplitude parallel reflections are occasionally interrupted by thicker transparent packages that generally lack consistent internal reflectors, but transition to chaotic acoustic facies with hummocky surfaces as profiles approach the basin slope and fluvial deltas (e.g., Figure 3). Gravity cores show that the top  $\sim 1.5$  m of sediment consists of 0.5-10 mm thick laminated couplets (hereafter referred to as couplets), which are composed of alternating grey-brown to grey, coarse-grained bases (typically silt sized), that grade into light-grey fine-grained caps (typically clay sized). In general, the contact between an underlying fine-grained cap and an overlying coarse-grained basal unit is sharp. In all the lakes surveyed, the boundary between individual couplets is relatively clear in the proximal basins but becomes more diffuse in the distal basins, especially with recent deposits in the top  $\sim 15$ -30 cm.

Thicker (relative to the couplets), coarser-grained (fine sand to silt) event deposits, often rich in organic detritus and typically normally graded with sharp, sometimes erosive bases, interrupt the laminated background sediment. For each lake below, a brief description of the acoustic stratigraphy and sediment character is provided before focusing on the record in the top  $\sim 40$  cm of sediment, which contains evidence of the recent events (both climatic and seismic). We assign event deposit identifiers independently at each lake, which do not necessarily correspond to the same event deposit identifiers within other lakes (e.g., the Sk1, Sk2, Sk3... deposit at Skilak Lake may not be the same as Tu1, Tu2, Tu3... at Tustumena Lake). Event deposit identifiers are ordered chronologically (i.e., Sk1 is the youngest deposit identified at Skilak Lake).

#### 4.1.1. Skilak Lake

Twenty-eight cores and 58 line-km of Chirp data were collected on Skilak Lake in 2020 and 2021 (Figure 2). Chirp profiles show the 1964 megaturbidite and MTD complex (as well as older MTDs) (Praet et al., 2017) expressed as thick transparent acoustic packages (Figure 3). The post-1964 stratigraphy is made up of parallel, high-amplitude reflections with no observable indicators of mass transport deposits (Figure 3). In sediment cores, this post-1964 section shows couplets (average thickness  $\sim 0.5$  cm) interpreted as varves (Figures 3 and 4) (Boes et al., 2018) that are punctuated by thicker, normally graded event deposits ( $> \sim 1$  cm), often with coarser bases and a slightly darker brown color than the background varves. From the top of the SK20-cores (collected in August 2020), eight dark winter caps can be counted in the CT-scans down to the top of a turbidite that correlates well with a turbidite observed in the top of Boes et al. (2018) cores (collected spring/summer 2012), indicating that deposition in Skilak Lake has been continuous since 2012 (Figure 5). We identify six event deposits in Skilak Lake (Sk1-Sk6) that are described below.

The thickest deposit observed in Skilak Lake (Sk5) represents the 1964 megaturbidite (Praet et al., 2017; 2022), which exhibits high spatial variability (Figures 4, 6B, and 7), and a light grey to brown-grey color with a sandy basal unit and erosive lower contact in the proximal basin (Figure 3 and 4). Due to the large thickness of Sk5 in the proximal basin (8-79 cm), only six cores sampled the pre-1964 sediment, which includes Sk6, a 1.8-6.2 cm-thick deposit with a very fine sand to silt base and light brown-grey color (Figure 4). Although the erosive nature of the Sk5 basal contact introduces uncertainty, Sk6 appears to be  $\sim 7$ -9 varve-years older than Sk5, and in co-located cores Praet et al. (2022) interpreted the Sk6 equivalent deposit to record a  $M_w$  6.8 1954 intraslab earthquake.

In Skilak's proximal basin, the top 25 cm of sediment contains varves and event deposits over the last  $\sim 28$  years (Figure 5). Within this time frame, event deposits Sk4 and Sk3, span the 1995 to 1997 and 2009 varve years, respectively. Both Sk3 and Sk4 have similar characteristics such as thickness ( $\sim 1$  cm average) and

a brown to grey-brown silty base in cores near the fluvial inputs (e.g., in core SK20-08A; Figure 5). Sk3 and Sk4 become increasingly grey-brown towards the distal portion of the proximal basin (e.g., SK20-10A; Figure 5), but maintain a relatively uniform thickness across the basin (Figure 6B and 7). The base of Sk3 and Sk4 contain organic detritus in cores adjacent to fluvial inputs (e.g., SK21-01A; Figure 4). Multiple coarse (high radiodensity) laminae within the Sk3 and Sk4 deposits are observed in CT-scans (SK20-08A, Figure 5).

The two most recent event deposits occurred within the 2016 varve year (Sk2) and the 2018 varve year (Sk1) and share common characteristics including normal grading and a lighter grey to brown-grey color (relative to Sk3 and Sk4). Sk1 and Sk2 exhibit a ponding geometry and are significantly thicker in the middle of the proximal basin when compared to their thicknesses towards the basin edges or in the distal sub-basin (Figure 6b and 7). However, there is a slight localized increase in thickness for both Sk1 and Sk2 towards the southeastern basin slope (17 and 26 mm, respectively; Figure 7). In the distal sub-basin where the varve boundaries become diffuse, Sk1 and Sk2 can be difficult to distinguish but are identified based on their relatively high radiodensity compared to background sediment (Figure 4).

Near the main fluvial deltas, Sk1 and Sk2 consist of a fine sand basal unit that grades into a silty-clay top, which is similar in grain size to background sediment (Figure 6a). Adjacent to the Skilak River delta (i.e., SK21-01A), the grain size distribution of the basal component of both Sk1 and Sk2 consists of more than 25% very-fine to fine sand and grades rapidly to dominantly silt size at the top of the deposit (Figure 6a). At increasing distance from the Skilak River delta the grain size distribution becomes finer, to a point in which the basal unit is 80% fine-silt (i.e., SK20-03A in Figure 6a) and exhibits a lighter grey-brown color (SK20-10A; Figure 5). The D50 values also show a sharp peak in the basal component that rapidly decays to background levels and mimics the overall fining with distance from fluvial inputs. The grain size distributions of Sk1 and Sk2 are coarser and fine more quickly than Sk3 (or Sk4) (Figure A2).

Slight variations in the sedimentological character of specific Sk1 and Sk2 deposits are observed and may reflect variation in sediment sources. The basal component of Sk1 and Sk2 in core SK20-02A, and Sk1 in core SK20-09A (both cores are in the center of the proximal basin, Figure 2), is more grey to bluish-grey in color compared to the typical brown-grey observed in adjacent cores (e.g., Sk1 in SK20-09A vs SK20-08A) (Figure 5). The thickness of this grey basal unit is ~5 mm for Sk1 in both cores, and ~1 cm for Sk2 in SK20-02A and displays inverse grading in both CT-scans and grain size profile. A return to normal grading in both CT-scans and grain size is observed in the overlying brown-grey portion, giving the overall deposit an inverse to normal grading character (Figure 5, 6a). The cross-lake transect centered on SK20-02A (i.e., E-E' in Figure 4), shows a significantly thinner (<2 mm) grey basal component for the two deposits (Sk1, Sk2) in the cores near the basin slope, which is thicker in core SK21-09A located adjacent to the southeastern slope.

Variations in the couplets associated with Sk1 and Sk2 may relate to the timing of deposition. The varve year clay caps associated with Sk1 and Sk2 appear less well-developed than other winter clay caps. For example, in core SK20-02A, the clay cap associated with Sk2 (i.e., the clay cap directly above) is faint in CT-scans when compared to the clay caps above and below, and more difficult to distinguish from the background silty sediment (Figure 5b). Similarly, a very thin (<1 mm), low radiodensity lamina is present just prior to the deposition of Sk1 in SK20-02A, the deposit is then followed by a relatively well-developed clay cap (Figure 5b). The weakly developed clay caps indicate deposition later in the varve year and are used later to constrain the triggering event.

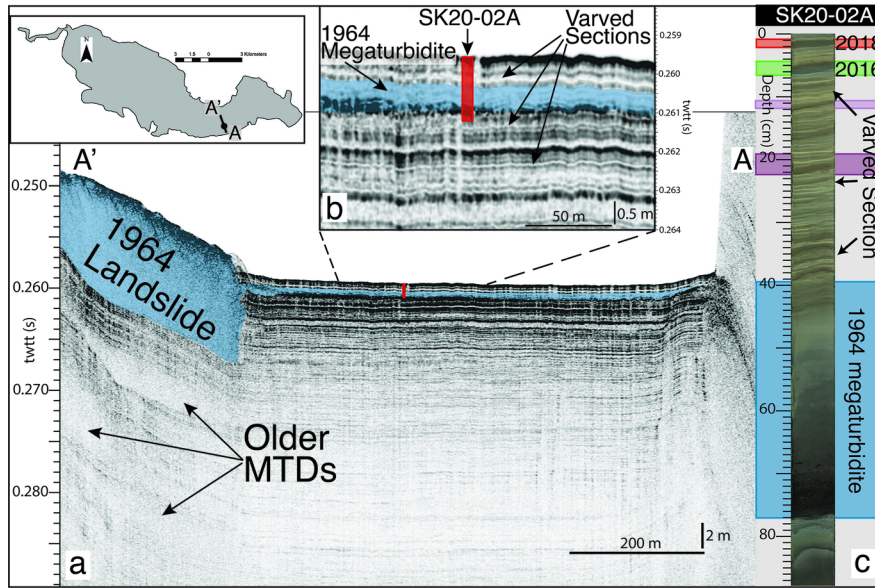


Figure 3: (a) Chirp profile (SK20-08) from Skilak Lake with high-amplitude parallel reflections interrupted by larger transparent homogenous packages. (b) Chirp inset of upper 3 m with location of core SK20-02A (red rectangle). (c) Core SK20-02A showing varved sediment and event deposits.

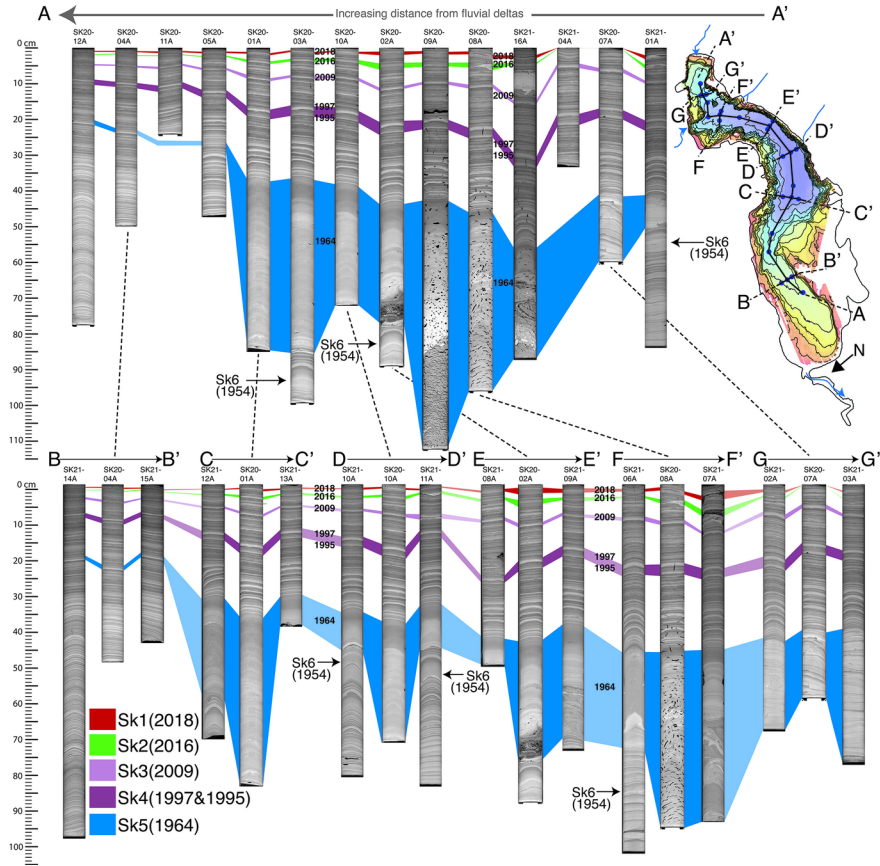


Figure 4: CT-scan transect of Skilak Lake cores. The background varve sedimentation is seen as laminated sediment couplets and the larger event deposits are mapped. The 2018, 2016, and 1964 earthquake-triggered turbidites exhibit rapid thinning adjacent to basin slopes (e.g., profiles D-D' and E-E'), as well as away from the inflow proximal basin (e.g., A'-A). The 1995-1997 and 2009 flood turbidites exhibit a more uniform thickness across the basin.

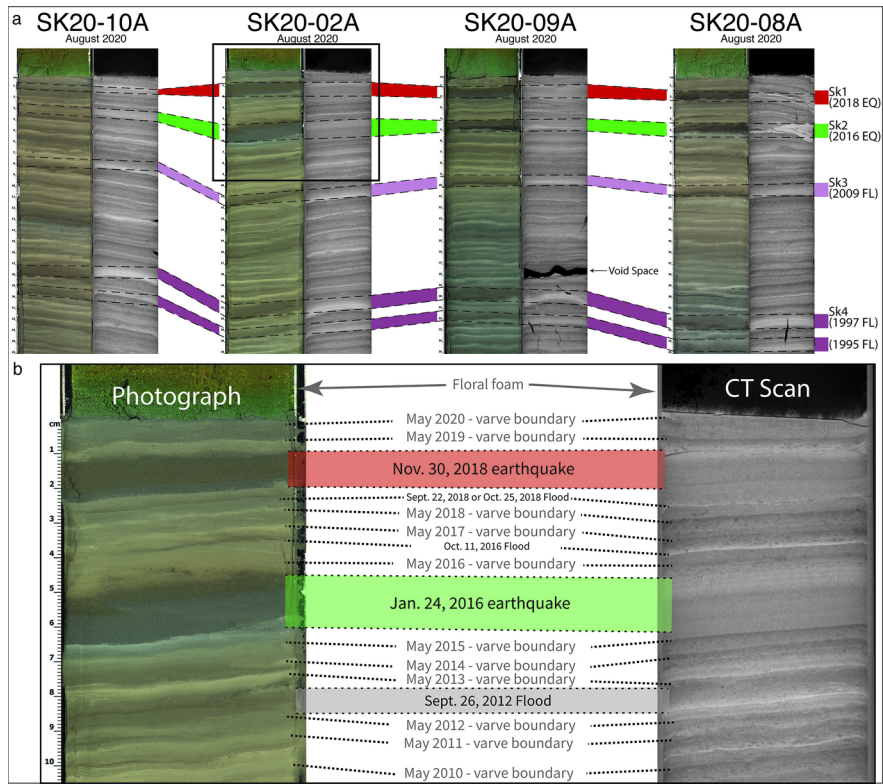


Figure 5: (a) High-resolution photographs and CT-scans of four cores from Skilak's central basin (see Figure 2 for locations). Black box is location of part b. (b) Lower panel shows the top of core SK20-02A. In photographs, a typical varve year couplet is expressed as darker coarse-grained summer base and a light-colored fine-grained winter cap.

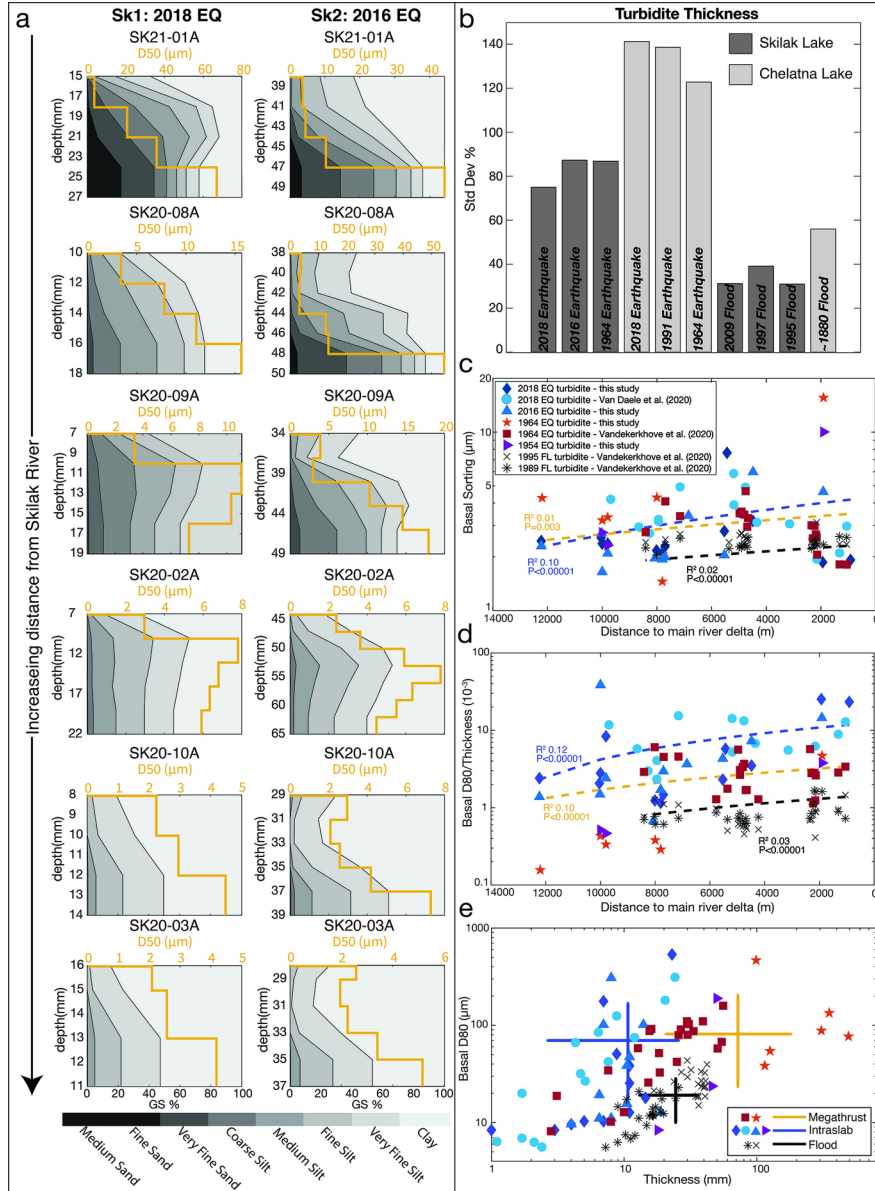


Figure 6: (a) Grain size evolution through the 2018 (left column) and 2016 (right column) earthquake turbidites from six cores in Skilak proximal basin (see Figure 2 for locations). (b) Turbidite thickness variation for mapped turbidites in Skilak and Chelatna Lakes. (c) Basal sorting vs distance from fluvial source from select cores in all study sites. (d) Ratio of basal D80 to thickness vs distance from fluvial source from select cores in all study sites. (e) Basal D80 vs thickness from select cores in all study sites. Skilak Lake data are represented by stars (megathrust events) and diamond/triangles (intraslab events). Eklutna Lake data are represented by squares (megathrust events) and circles (intraslab events) and are taken from Vandekerhove et al. (2020) and Van Daele et al. (2020).

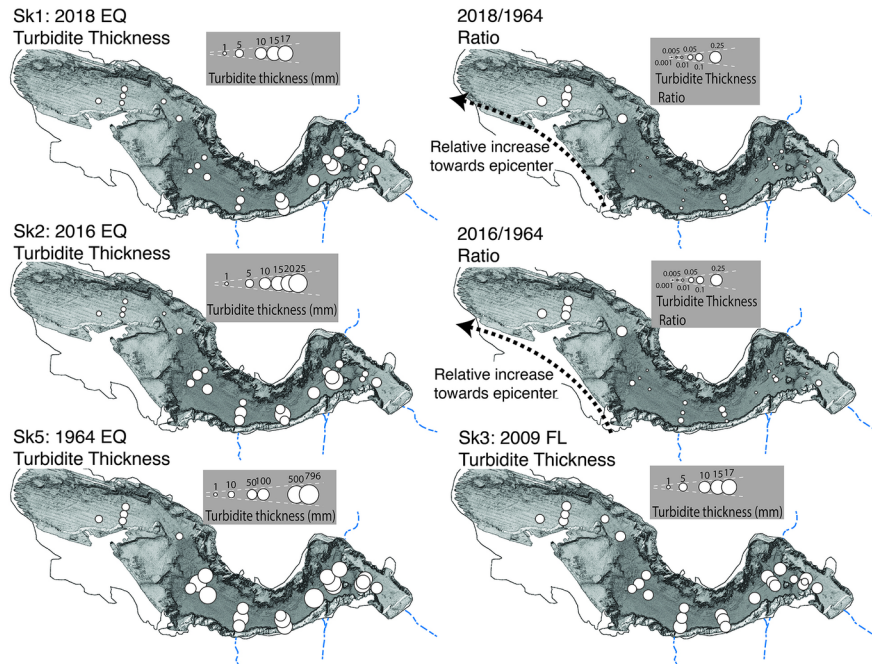


Figure 7: Thickness distribution of turbidites observed in Skilak Lake cores. Ponding geometry characteristic of seismically triggered turbidites is observed in the 2018, 2016, and 1964 deposits. In contrast, the 2009 flood deposit has a more uniform thickness across the lake basin. Relative to the 1964 deposit, the 2016 and 2018 turbidites are thicker in the distal basin, as seen in the thickness ratio, suggesting a possible sensitivity to epicentral directionally.

#### 4.1.2. Kenai Lake

Seventeen gravity cores and 34 line-km of Chirp data were collected in Kenai Lake along the long-axis of the lake, with two additional cross-lake profiles in 2020 and 2021 (Figure 8). Cores from the eastern end of the lake, near the Snow and Trail River deltas, reveal thick (~1 cm) varves that are frequently composed of multiple high radiodensity laminae (Figure 8). In the proximal basin 56 winter varve caps can be counted in cores to the top of the 1964 megaturbidite (e.g., Ke1, Figure 8), confirming that sedimentation in Kenai Lake is continuous on an annual basis (Praet et al., 2017; Boes et al., 2018). In addition to the 1964 megaturbidite, several climatically generated turbidites have been previously identified in co-located cores from the proximal basin (Boes et al., 2018) (Figure 8). In the distal basin, varves thin significantly (<0.3 cm thick) and separating individual varves is challenging (Figure 8).

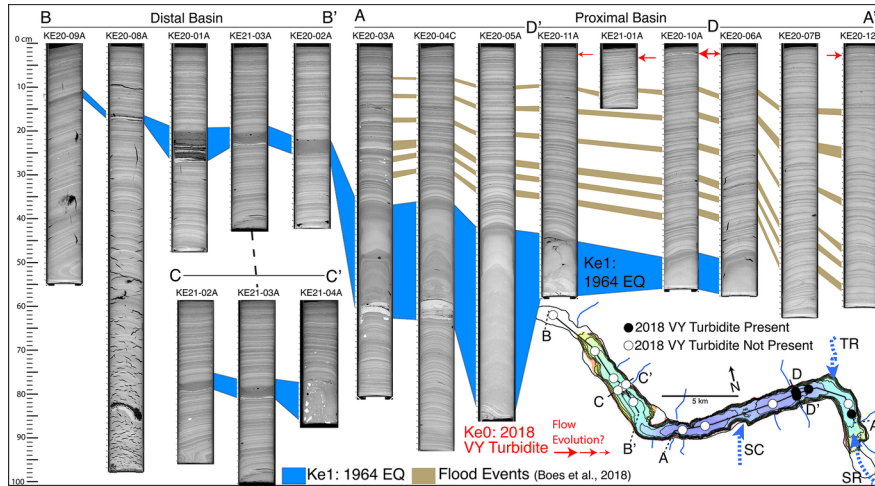


Figure 8: CT-scan transect of Kenai Lake cores. Varves and event deposits are thick in the eastern part of the lake adjacent to the Snow (SR) and Trail (TR) rivers. Possible event deposits in the 2018 varve year are observed in a limited localized region near auxiliary fan deltas. SC = Ship's Creek.

Beyond the previously identified deposits, the only additional event deposit is a 2-3 mm thick medium- to fine-sand and silt lamina (Ke0) in the upper-middle portion of the 2018 varve year couplet that is restricted to cores adjacent to an auxiliary fan delta near the Trail River delta (i.e., Ke0 at ~1.5 cm depth in KE20-10A, Figure 8 and 9). Ke0 thins rapidly away from the auxiliary fan delta to <0.5 mm thickness in KE21-01A and KE20-11A (i.e., D-D' transect, Figure 8), and is not evident ~2 km away towards the middle of the basin in KE20-05A. Nearest the Trail River delta, in core KE20-06A this deposit is organic rich with individual organic fragments visible in CT scan (and photograph) and lacks a sand-silt basal component. A similar deposit, but with noticeably finer basal grain size (silt size only), also within the 2018 varve year, is present in core KE20-12B near the Snow River delta but is not apparent ~800 m away in KE20-07B (Figure 8).

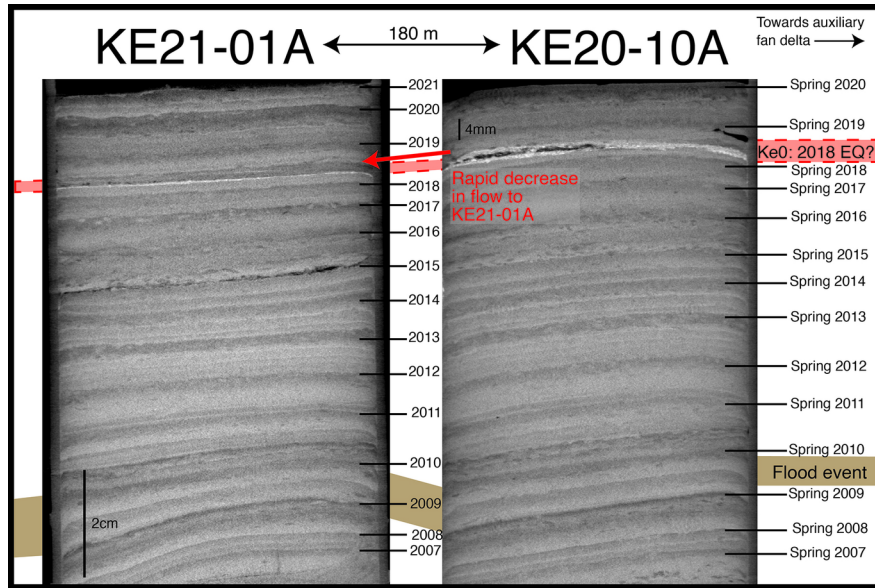


Figure 9: Upper 10 cm of cores KE21-01A and KE20-10A showing possible 2018 earthquake lamina (Ke0) in Kenai Lake. The anonymously high radiodensities and rapid thinning of Ke0 between cores is suggestive of deltaic slope failure. For core locations see Figure 8.

#### 4.1.3. Tustumena Lake

Seven cores and 10 line-km of Chirp data were collected from the proximal basin and a distal sub-basin in Tustumena Lake in 2020 and 2021 (Figure 10 and 11). In the proximal basin, Chirp data show a hummocky lake bottom with possible MTD blocks and chaotic, discontinuous internal reflections near the basin slopes (Figure 10). A thick (1-2 m) acoustically transparent unit is observed at a depth of  $\sim 0.5$  m below the lake floor near the northern slope that transitions to a more organized seismic facies with resolvable internal reflections and a ponding geometry closer to the depocenter. Below this unit, additional thinner ( $< 0.5$  m) acoustically transparent packages also exhibit a ponding geometry within the depocenter.

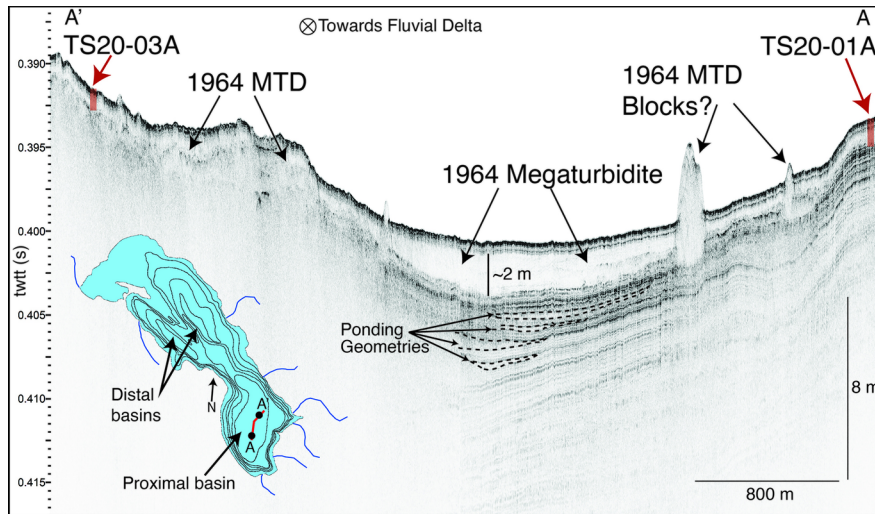


Figure 10: Chirp profile (TS20-01 and TS20-02) from Tustumena's proximal basin (red line of inset map). Effects of the 1964 earthquake include a ~2 m thick megaturbidite and chaotic reflectors with hummocky surfaces near the basin slopes. Red squares mark the location of cores TS20-03A and TS20-01A.

A transect of four cores in the proximal basin and three cores in a distal sub-basin show that the background sedimentology of Tustumena Lake is composed of couplets that average about ~5 mm in thickness (Figure 11). The couplets exhibit a grey-brown, sandy-silt basal component and a light-grey, clay cap (Figure 12). Cores located near fluvial inputs exhibit higher amounts of organic material (e.g., TS20-05A) and thicker, coarser deposits (e.g., TS20-03A and TS20-04A). A Cs-137 profile for Tustumena Lake was constructed from core TS20-06A in the distal basin at 2 cm intervals and shows a spike at the 10-12 cm depth interval that rapidly decays to non-detectable levels by 16 cm depth (Figure 11).

Three event deposits that range in thickness from ~0.1-53 cm are mapped in cores across Tustumena Lake. In cores from the proximal basin, Tu3 is seen as a ~14-53 cm thick deposit (Figure 11), that corresponds to the thick, transparent unit observed in seismic section (Figure 10). Tu3 consists of a grey to brown-grey, medium to fine-sand base with a sharp erosive lower contact that grades upwards to a finer-grained section containing occasional ~1-5 mm silt to very-fine sand laminae and is capped by a clayey-silt top. In core TS20-03A, Tu3 overlies a section of couplets with apparent convolute bedding (Figure 12). In the distal basin, Tu3 is thinner (5-15 cm thick), though still consists of a fine sand base and clay top, but above the basal section lacks the internal laminae observed in the proximal basin (Figure 11). In the proximal basin, the couplets directly above Tu3 are thicker than the background steady-state couplets (e.g., at 20-25 cm depth in TS20-01A, Figure 11).

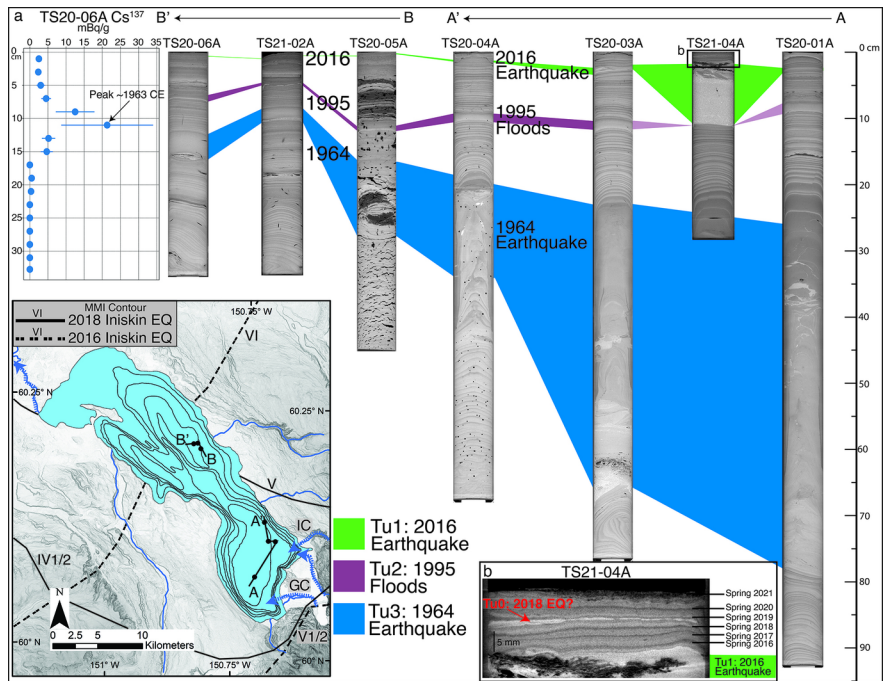


Figure 11: (a) CT-scan transect across Tustumena Lake with Cs-137 profile. Deposits are thick and coarse in the proximal basin, especially near Indian Creek (IC) and Glacial Creek (GC). The 1964 and 2016 event deposits are associated with sedimentary structures that indicate high flow velocities, including convolute bedding (i.e., below T3 in TS20-03A) and rip up clast (i.e., top of T1 in TS21-04A). Bathymetry contours in inset map are 50 m from ADF&G (2015). (b) Top 3 cm of TS21-04A showing evidence of localized slope failure deposited late in the 2018 varve year, likely the result of the 2018 Anchorage earthquake.

In the proximal sub-basin, the 1963 CE peak in Cs-137 suggest that the upper ~15 cm of sediment correlates to deposition over the last ~30 years (Figure 11 and 12). Within this section, Tu2 is a prominent event bed that maintains a relatively uniform thickness (~0.5-1.5 cm) across the lake. Tu2 consists of a brown to grey-brown very-fine sand to silt base (~0.5 cm thick) that transitions to grey silt and light grey silt-clay top (Figure 12).

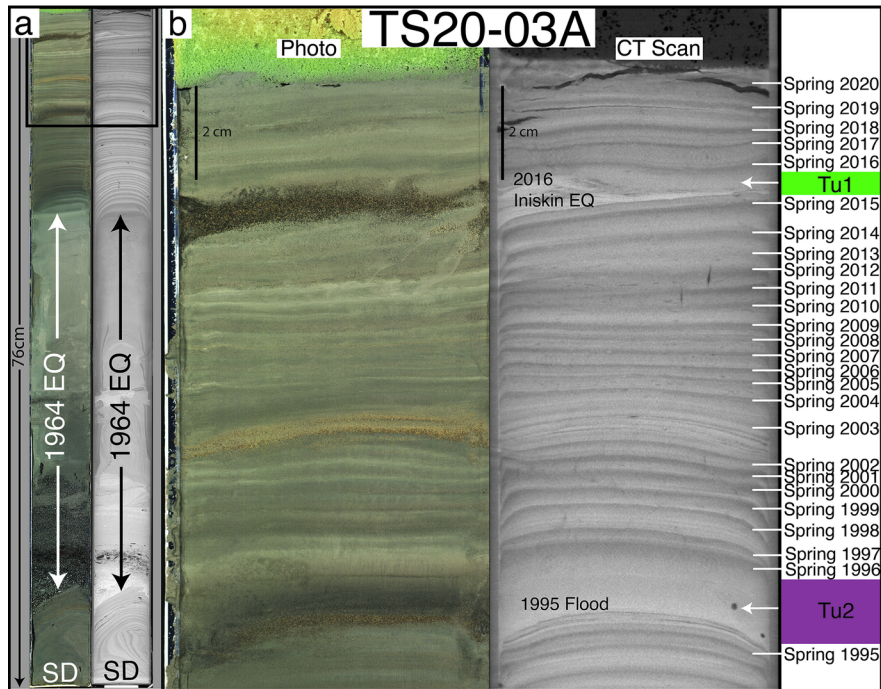


Figure 12: (a) High-resolution photograph (left) and CT-scan (right) of core TS20-03A (see Figures 10 and 11 for location). Black box at the top represents area of part b. SD=Slump Deposit. (b) Top ~12 cm of TS20-03A. Event deposits T1 and T2 interrupt the background varves, and the coarser nature of T1 relative to T2 is clearly seen in the high-resolution photograph (and CT-scan).

The base of the next event deposit, Tu1, is located at a depth of ~3 cm in the proximal basin (Figure 12). Tu1 is thickest in the proximal basin (9 cm) and thins significantly towards the distal sub-basin (< 1 mm) (Figure 11). The thinning of Tu1 below 1 mm prohibits easy identification in the distal sub-basin, nevertheless it is identified based on its higher radiodensity in CT-scans relative to the background sediment (Figure 11). In the proximal basin, the basal component of Tu1 is thicker and coarser than the background couplets (fine sand vs silt) and other observed event deposits (i.e., Tu1 vs Tu2, Figure 12). Near fluvial inputs this base is composed of fine to very-fine sands with incorporated organic material, and in TS21-04A, Tu1 is thicker, coarser-grained (medium sand), and the basal contact is erosive appearing to have removed the lower Tu2 deposit (Figure 11). The top of the basal component for Tu1 in TS21-04A contains clasts of background sediment with clear couplets preserved and likely represents a rip-up clast.

Additionally in core TS21-04A, which is the most proximal core to a major fluvial input in Tustumena Lake (e.g., Indian Creek, Figure 11), the top 2 cm of sediment contain a 1-1.5 mm thick deposit (Tu0) that exhibits higher radiodensity (silty-sand) than background couplets (Figure 11b). Tu0 appears to have been deposited during clay cap formation with low radiodensity lamina observed both above and below. Due to the thin nature of the deposit, it is difficult to identify any distinguishing sedimentological features beyond the relatively coarse character (high radiodensity). A correlative deposit may be present in TS20-03A, however deposit thinning (thickness <0.5 mm), and decreasing grain size make identifying a distinction from background couplets uncertain and prohibit a confident correlation (Figure 12).

Using a combination of lamination counting (couplets) and Cs-137 dating, we developed an age model with annual resolution for Tustumena Lake. The 1963 CE Cs-137 peak occurs at the top of T3 which is located 56 clay caps below the 2020 sediment-water interface, and an additional clay cap is observed in cores collected in 2021 (Figure 11). Together these observations indicate that sedimentation in Tustumena Lake is annual

and that the couplets represent varves, implying that Tu3 was deposited in the 1964 varve year. The 25 clay caps between the 2020 sediment-water interface and T2 indicate it was deposited in the 1995 varve year, and the 5 clay caps between the sediment-water interface and T1 suggest deposition in the 2016 varve year (Figure 12). The three clay caps between the 2021 sediment-water interface of TS21-04A and Tu0 indicated that it was deposited in the 2018 varve year.

#### 4.1.4. Chelatna Lake

Twenty-eight gravity cores and 141 line-km of Chirp data were collected at Chelatna Lake in June 2021. Chirp subbottom profiles in the basin center image high amplitude parallel reflections to a depth of 30 m that are punctuated by multiple acoustically transparent packages (Figure 13). The parallel reflectors appear to downlap away from the main fluvial input and onto the distal part of the main basin. The thickest transparent package (~4 m) is imaged at a depth of ~2.5 m in the center of the basin (Figure 13). Within this transparent package, an internal reflector exhibits a chaotic character and hummocky surface and thins away from the basin slope. In the top 2.5 m, two acoustically transparent units exhibit a ponding geometry in the middle of the basin and overlie reflections with relatively high amplitudes (Figure 13).

The background stratigraphy within the top ~1.5 m of sediment consists mainly of couplets that are composed of a grey, sandy-silt base that grades into a pale brown clay cap (Figure 14). The couplets in Chelatna are significantly thinner than in the other lakes, with an average thickness in the middle of the basin of ~1 mm. Couplets in the upper section of the cores appear thicker with more distinguishable boundaries that become thinner and more difficult to separate with depth. A Cs-137 profile was constructed from core CH21-09A at 1 cm intervals and shows a peak at a depth of 9-10 cm that rapidly decays to non-detectable levels by 14 cm depth (Figure 14).

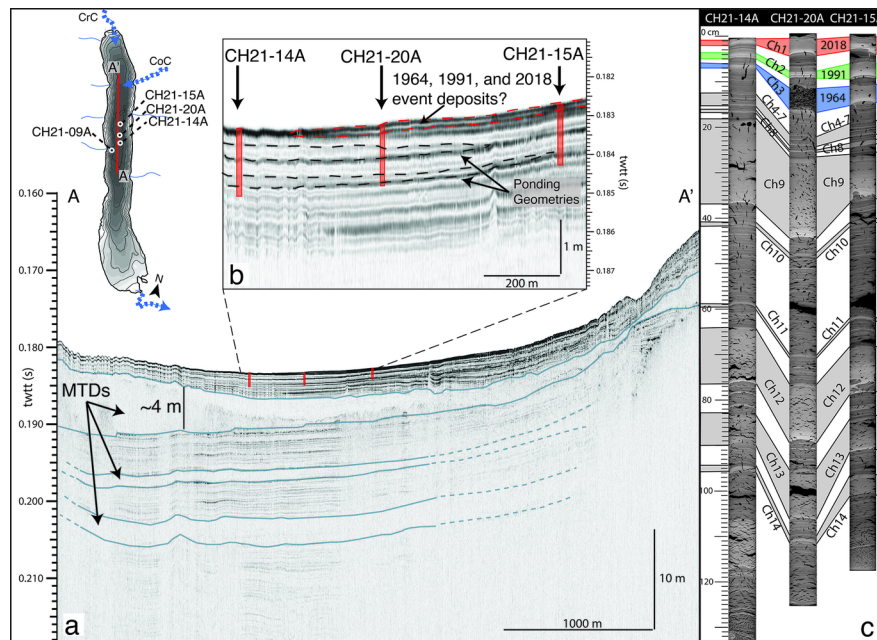


Figure 13: (a) Longitudinal Chirp profile (CH21-59) from Chelatna Lake. Inset map shows location of cores and Chirp profile. CrC=Cripple Creek; CoC=Coffee Creek. (b) A close-up of the central portion of the profile corresponding to coring depths (red squares) showing down-lapping reflectors (red dashed line). (c) Core CT-scans showing mapped event deposits. The 2018 (Ch1), 1991 (Ch2), and 1964 (Ch3) earthquake turbidites appear in the upper 15 cm of the cores.

At least 14 event deposits are identified in the top 1.25 m of sediment in Chelatna Lake that range in thickness from  $\sim 0.5$ -20 cm (Figure 13) and can be classified into two categories. The deposits of the first set, exemplified by Ch1, Ch2, and Ch3, appear light yellowish-grey to brownish-grey, are relatively coarser grained (fine sands to silt) (Figure 14), exhibit upward decreasing radiodensity and MS, and show variable thickness across the basin (Figure 6b). Several of the larger deposits in the first set have erosive bases with rip-up clasts that consist of the background couplets (i.e., Ch9 and Ch12, Figure 13). The second set, of which Ch4, Ch5, and Ch7 are representative, are grey to dark grey clayey-silt deposits, similar in color to the basal section of the background couplets (Figure 14) and exhibit a uniform thickness across the basin (Figure 6b).

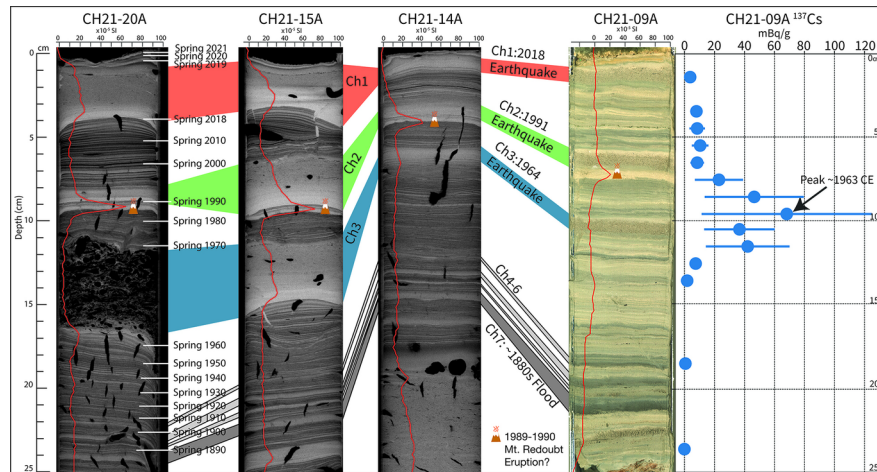


Figure 14: CT-scans of cores CH21-20A, CH21-15A, and CH21-14A and high-resolution photograph of CH21-09A with MS curve (red line). To the right, the Cs-137 profile constructed from CH21-09A shows a peak in values at the top of Ch3. Air pockets (sub-vertical black voids) from expanding gas are visible in the CT-scans.

Based on the location of the 1963 CE peak in Cs-137, the top 20 cm likely represent  $\sim 100$  years of accumulation (Figure 14); within this interval, seven event deposits are identified (Ch1- Ch7). Ch4, Ch5, and Ch7, belong to set two and increase in deposit thickness with core depth. The deposit character is best observed in the stratigraphically lowest, and thickest Ch7 (average 0.5 cm), which is composed of dark grey very fine silt that grades to a pale grey silty-clay top. Located within this grouping of dark grey deposits, Ch6 is a thin (max thickness  $\sim 0.5$  cm) brownish-grey normally graded unit best recognizable in CT-scans and interpreted to belong to deposit set one (Figure 14).

The three most recent event deposits (Ch1, Ch2, Ch3) are noticeably different in character from Ch7 and belong to deposit set one (Figure 14). The basal unit can be significantly lighter grey in color and coarser grained (sand) near the fluvial inputs. Organic fragments are present towards the middle and top sections of all three deposits, and a localized increase in macroscopic organic matter is observed for Ch3 in core CH21-20A (Figure 14). Below the deposits ( $\sim 1$ -2 cm depth) small scale microfractures and fissures infilled with overlying coarse-grained material (sourced from the overlying event deposit) are observed in some locations (e.g., Ch1, Ch3 in CH21-15A; Figure 14). Directly below Ch2 is a noticeably large spike in the MS data that corresponds with a relatively thick (2-5 mm) pale yellow unit with high radiodensity that is suggestive of a tephra deposit and is separated from Ch2 by a low-radiodensity lamina ( $\sim 2$  mm thick) (Figure 14).

Even though the thin character of couplets observed in Chelatna Lake introduces some uncertainty into lamination counts, an age model with annual resolution can be constructed from the combination of lamination counting and Cs-137 dating. The good correlation between the number of clay caps above Ch3 ( $57 \pm 1$ )

and the 1963 CE peak in Cs-137 suggests that the couplets are annual (varves) and indicates that Ch3 was deposited between the 1963-1965 varve years. We interpret the 141 clay caps (+/- 12) between Ch7 and the 2021 sediment water interface to suggest deposition sometime around the 1880s. Ch2, and the underlying deposit with anomalously large MS values, are located 30 and 31 clay caps below the 2021 sediment-water interface and would therefore have been deposited in the 1991 and 1990 varve years, respectively. Lastly, the three winter clay caps between Ch1 and the 2021 sediment-water interface suggest deposition during the 2018 varve year (Figure 14).

## 4.2 Fjord Stratigraphy and Sedimentology

### 4.2.1 Passage Canal

We collected four gravity cores and 11 line-km of Chirp data in Passage Canal in 2020. The background seismic stratigraphy consists of parallel high-amplitude reflections separated by irregular low-amplitude semi-transparent packages (~2-10 m thick) that often include a basal set of low- to medium-amplitude finer scale reflections (Figure 15). The acoustic stratigraphy maintains a relatively uniform thickness across the Trinity Flats basin, but several of the deeper semi-transparent packages do contain internal reflections with hummocky surfaces. The high-amplitude units that separate the larger semi-transparent packages appear to on-lap the Gradual Point Moraine (Figure 15). The uppermost unit in Chirp data is a ~5-7 m thick medium- to high-amplitude chaotic package with a hummocky surface in the west-southwest that transitions to a largely acoustically transparent unit with an internal chaotic reflector, this internal reflector thins towards the distal part of the basin. This upper package corresponds to the 1964 MTD and megaturbidite as mapped by Haeussler et al. (2014).

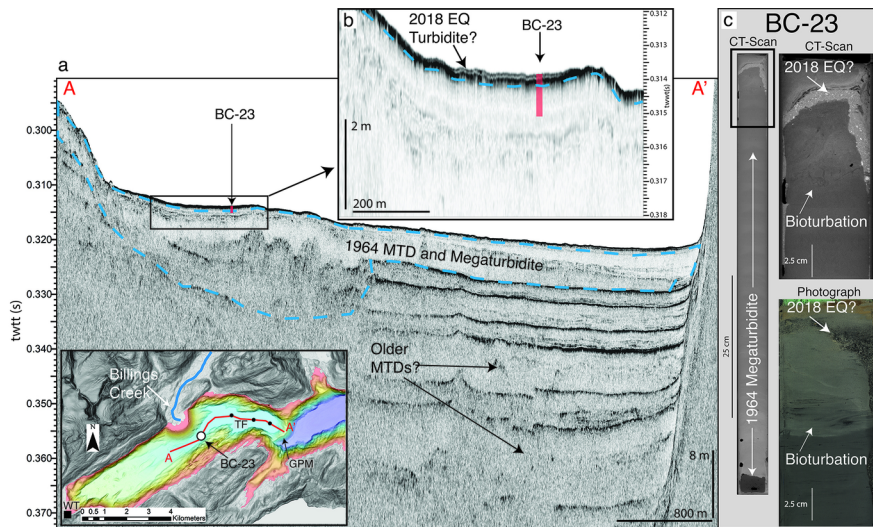


Figure 15: (a) Chirp profile Line-65 in Passage Canal. The hummocky surface, chaotic character, and large thickness of the 1964 MTD and megaturbidite identified by Haeussler et al. (2014) are mapped (blue dashed line). Inset map shows Passage Canal bathymetry from Haeussler et al. (2014) with Line-65 (red line) and cores (black dots). WT=Whitter; TF=Trinity Flats; GPM=Gradual Point Moraine. (b) The enlarged section of Line-65 located adjacent to the Billings Creek fan showing thin transparent reflector above the 1964 deposit which potentially corresponds to a coarse-grained unit observed in core BC-23. (c) Core BC-23, with enlarged section (black box) showing 2018 earthquake turbidite that rapidly buries bioturbation structures.

Near Billings Creek fan, the 1964 MTD and megaturbidite appear to be capped by a thin veneer of sediment that appears to pond in a bathymetric low (Figure 15). Within the bathymetric low, core BC-23 sampled

the top of 1964 megaturbidite and post-1964 deposits, the bottom 77 cm are composed of blue-grey fine silt that grades to clayey-silt with 5 cm of abundant bioturbation towards the top of core (Figure 15). The majority of core BC-23 is composed of homogenous sediment with some internal laminations concentrated at the bottom of the core and decreasing in frequency upward. At the very top of the core a ~3-cm-thick deposit abruptly buries the bioturbation structures that developed post-1964 and is composed of a medium- to fine-sand basal unit that grades upward to a clayey-silt middle and cap with small amounts of organic material. The basal contact of the sandy deposit is erosive (Figure 15), and the deposit thins abruptly basinward to a thickness 2.5-6 mm in the adjacent cores to the east. This deposit and its characteristics (sandy base with normal grading and internal laminae) is anomalous in the post-1964 deposition throughout the Passage Canal cores. The stratigraphic position together with the rapid burial and lack of reoccupation of benthic organisms indicates that this sandy deposit is recent, likely occurring within the last 3-5 years (of 2020 core recovery) (Dernie et al., 2003; Frojan et al., 2011; Waye-Barker et al., 2015).

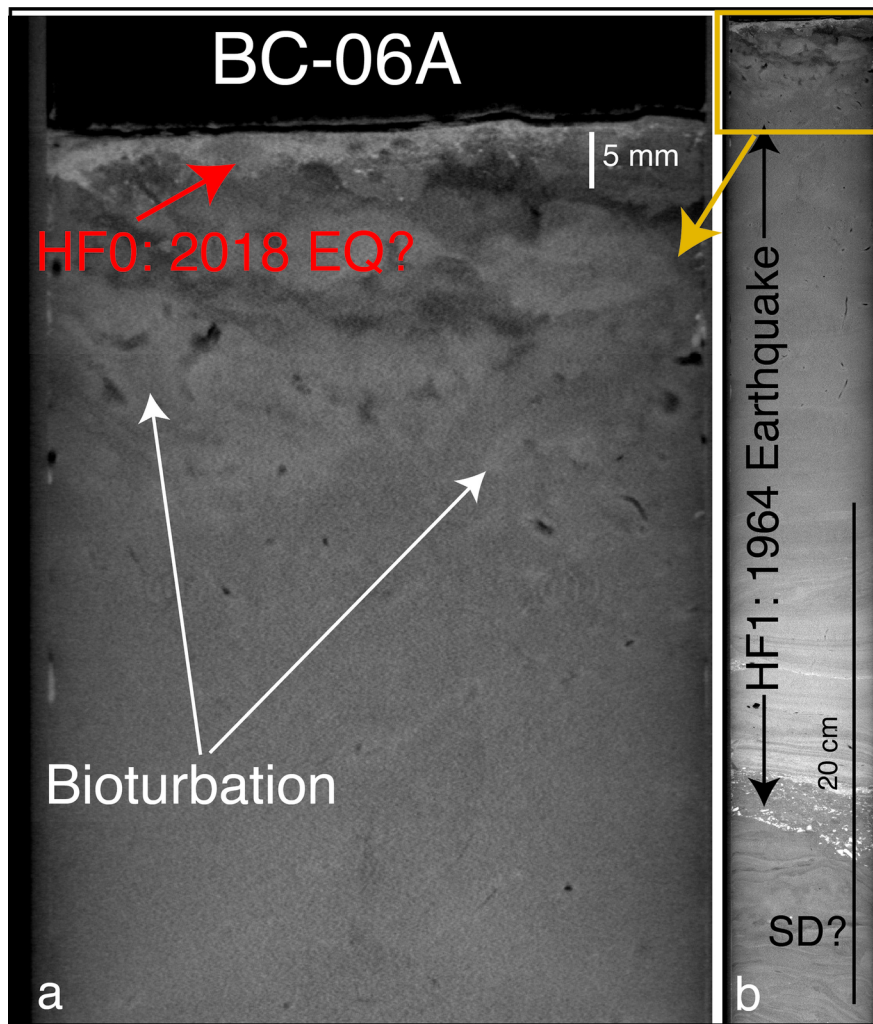


Figure 16: (a) Upper ~8 cm of core BC-06A (CT-scan) from Harriman Fjord. Bioturbation structures developed in the top of the 1964 megaturbidite and are rapidly buried by a high radiodensity (fine sand) lamina, which is interpreted to be the result of the 2018 earthquake. (b) Top 50 cm of BC-06A (CT-scan) showing 1964 earthquake deposit and background stratigraphy. Gold box corresponds to location of part a of this figure.

### 4.2.2 Harriman Fjord

A set of three gravity cores were collected in the proximal (southwest) basin of Harriman Fjord (i.e., adjacent to the Harriman Glacier) (Figure 1). The stratigraphy of Harriman Fjord is very similar to that of Passage Canal and is dominated by glacially sourced bluish-grey clayey-silt. Core BC-06A is located in the middle of the fjord and adjacent to a small auxiliary fan delta. The upper 50 cm of BC-06A shows a ~30 cm thick normally graded deposit (HF1), which correlates with similar deposits in other Harriman Fjord cores, and consists of a coarse-to-medium sand base with alternating fine and coarse lamina, that grades to a more massive homogenous middle and top section (Figure 16). Above this deposit in the upper ~10 cm of sediment, bioturbation structures are observed to reoccupy the fjord floor. A 2-3 mm thick, high radiodensity (fine sand to silt) lamina (HF0) is present at the top of BC-06A and observed to bury the bioturbation structures. The high radiodensities and fine sands of HF0 are anomalous in BC-06A, except for the lamina in the basal section of HF1 (Figure 16). The location of HF0 at the very top of the core suggests recent deposition.

## 5. Discussion

### 5.1 Event Deposit Origins – Climatic vs Seismic Triggers

The characteristics of the event deposits identified in this study are consistent with deposition from gravity driven turbidity flows (i.e., normally graded deposits that fine away from slopes) (Beck, 2009; Talling, 2014; Van Daele et al., 2017; Vandekerhove et al., 2020). The external trigger that initiated the turbidity flow and subsequent turbidite (climatic vs seismic), can be determined through sedimentological features related to flow characteristics (Vandekerhove et al., 2020). Basal grain size statistics (a proxy for flow velocity) (Figure 6c-e), deposit color (a proxy for organic content) (e.g., Figure 5, 12, 14, and 15), and spatial variations in deposit thickness (a proxy for source of remobilized sediment) (e.g., Figure 6b and 7), are among the most reliable diagnostic features in proglacial lakes (Vandekerhove et al., 2020), and are used to separate triggering mechanisms of the identified turbidites (Table 1).

We interpret, with high confidence, several turbidites to record strong ground motion during the 2018 Anchorage earthquake in Skilak Lake (Sk1), Chelatna Lake (Ch1), and Passage Canal (PC1) (Table 1), in addition to the previously identified deposit in Eklutna Lake (Van Daele et al., 2020). Shared characteristics of these deposits that are consistent with a seismic trigger include a lighter color, especially away from the main fluvial sources (e.g., Sk1 in SK20-10A, Figure 5); a relatively coarser-grained basal unit (e.g., Sk1, Figure 6a; Ch1, Figure 14) including high basal D80 values and relatively poor basal sorting (Figure 6c-e); and spatially variable deposit thicknesses (Figure 6b), with a ponding geometry (Figure 7). The sharp grading and exponential profile of the grain size evolution through the deposit (e.g., Sk1 in SK21-01A, Figure 6a and PC1 Figure A1) suggests a rapidly evolving flow velocity consistent with slope failure by a seismic trigger (Vandekerhove et al., 2020). Soft sediment deformation structures (e.g., microfaults), features commonly associated with excess pore pressure during strong ground motion (Monecke et al., 2004; Avşar et al., 2016; Molenaar et al., 2022), are associated with Ch1 and support a seismic trigger (e.g., CH21-15A, Figure 14). The location of Sk1 and Ch1 in the 2018 varve year, as well as the weakly developed winter clay cap associated with Sk1 (suggestive of deposition in the winter months), is consistent with the timing of the November 30, 2018, Anchorage earthquake.

The external trigger of the thin (0.5-3 mm) silty-sand lamina adjacent to auxiliary fan deltas in Harriman Fjord (HF0), Kenai (Ke0) and Tustumena (Tu0) lakes are enigmatic, but several lines of evidence suggest slope failure via a seismic trigger in late 2018 (Figure 8, 11, and 16). The medium-to-fine sand of Ke0 is anomalously coarse in the post-1964 stratigraphy of KE20-10A, and together with the dramatic thinning and fining of Ke0 to nearby cores (Figure 9), is evidence of sediment remobilization from localized deltaic slope failure (Beck, 2009; Vandekerhove et al., 2020). Similar observations for Tu0 and HF0 (i.e., relatively coarse grain size and evidence of rapid flow evolution, Figure 11b and 16a) suggest that these deposits are also the result of a localized delta slope failure. In Kenai Lake, there is evidence of elevated mean daily discharge in the hydrodynamically connected Kenai River during the autumn of 2018, however the flow rate is smaller than previous years in which a similar coarse-grained deposit was not produced (e.g., 2009 and

2012 varve years, Figure A4, Stream Gauge USGS 15266110, USGS (2021)). With a known external trigger in 2018 produced by the 2018 Anchorage earthquake, strong ground motion is the most likely cause of slope failure and the subsequent deposits. The location of Ke0 and Tu0 within the overall varve year also supports failure during the November 30, 2018, Anchorage earthquake, especially for Tu0 where a low radiodensity lamina brackets the deposit (Figure 11b). Similarly, the position of HF0 at the very top of the core with little overlying sedimentation supports recent deposition. Therefore, we interpret Ke0, Tu0, and HF0 to be the result of highly localized sediment remobilization by strong ground motion during the 2018 Anchorage earthquake with moderate-to-high confidence.

We infer that the 2016 Iniskin earthquake triggered turbidity flows in Skilak (Sk2) and Tustumena (Tu1) Lakes (Table 1). Both deposits are relatively light in color and have coarser grained basal units (e.g., Figure 5, 6c-e, 12), with deposit thicknesses that are highly variable in both lakes (Figure 6b, 11), and Sk2 further exhibits a ponding geometry across Skilak Lake (Figure 7). Together these characteristics are consistent with a seismic origin (Vandekerhove et al., 2020). The grain size evolution through Sk2 exhibits the sharp grading and exponential profile (e.g., SK20-08A and SK20-09A, Figure 6a) consistent with rapid flow evolution by seismically induced sediment remobilization (Vandekerhove et al., 2020). In Tustumena Lake, erosion of underlying strata and inclusion of rip-up clast near the basin slopes in core TS21-04A (Figure 11) is potential evidence of a highly energetic flow (Talling, 2014), often associated with seismically induced slope failure (Vandekerhove et al., 2020). Deposition of Sk2 and Tu1 occurred in the 2016 varve year and are both associated with weakly developed winter clay caps suggesting emplacement during the winter months, consistent with the timing of the January 24, 2016, Iniskin earthquake.

Strong shaking during the 1964 earthquake left sedimentary evidence across a large swath of southcentral Alaska (e.g., Plafker, 1969; Brothers et al., 2016; Roland et al., 2020), including several of the basins examined in this paper (McCulloch, 1966; Haeussler et al., 2014; Praet et al., 2017; 2022). Based on similarities in stratigraphic depth and deposit character between co-located cores from previous studies, we interpret the megaturbidites observed in Kenai (Ke1, Figure 8) and Skilak (Sk5, Figure 4) Lakes to record shaking during the 1964 earthquake (Table 1) (Praet et al., 2017; Boes et al., 2018; Praet et al., 2022). The effect of the 1964 earthquake is well documented in Passage Canal (Haeussler et al., 2014) and the larger PWS region (Brothers et al., 2016; Roland et al., 2020), and we assign the large MTD and megaturbidites observed in Passage Canal and Harriman Fjord to this event (Table 1). In Tustumena Lake, the thick (>2 m), ponded, acoustically transparent facies of Tu3 is consistent with the characteristics of a megaturbidite triggered by strong ground motion (Bouma, 1987; Van Daele et al., 2014; Praet et al., 2017), and the correlation of Tu3 with the 1963 CE peak in Cs-137 along with the associated slump deposit (Figure 12), suggests that Tu3 records the 1964 earthquake as well (Table 1). We similarly interpret Ch3 in Chelatna Lake to record strong ground motion during the 1964 earthquake based on its correlation to the peak in Cs-137 (Figure 14), together with sedimentological characteristics indicative of a seismic trigger including associated soft sediment deformation structures (e.g., core CH21-15A, Figure 14) (Table 1).

The remaining turbidites identified in this study are not observed as widely across the study sites and we instead interpret these deposits as the result of external triggers (seismic, climatic, or volcanic) with more localized effects. Sk6 in Skilak Lake, has been identified in co-located cores as the sedimentary signature of the  $M_w$  6.8 1954 intraslab earthquake that occurred just north of Skilak Lake (Boes et al., 2018; Praet et al., 2022). The character of Ch2 in Chelatna Lake also suggests a seismic trigger (Table 1) and we interpret Ch2 to be the result of a  $M_w$  6.3 1991 reverse focal mechanism earthquake with an epicentral depth of 115 km that occurred directly below Chelatna Lake with estimated MMI of  $\sim$ IV1/2-V (USGS, 2016c). We interpret the small (2-5 mm) light-colored fine-grained deposit that lies directly below Ch2 with anomalously high MS values to be a tephra deposit from the 1989-1990 Mt. Redoubt eruption, whose ash cloud covered the Chelatna area (Mulliken et al., 2018).

We interpret a climatic trigger for the Sk3, Sk4, Tu2, and Ch7 deposits (Table 1). In co-located cores on Skilak Lake, Boes et al. (2018) correlate Sk3 and Sk4 with large spikes in precipitation on the Kenai Peninsula that occurred during the 1995, 1997, and 2009 varve years (Figure 5). Similarly in Kenai Lake, the

turbidites between the 1964 deposit and the 2012 varve year have an established climatic origin in co-located cores (Figure 8) (Boes et al., 2018). At Tustumena Lake, spikes in precipitation values at the nearby Homer weather station in 1995 support a climatic trigger for Tu2 (Figure 12) (Boes et al., 2018 and references therein). Lastly, in Chelatna Lake, the characteristics of Ch7 are consistent with a flood turbidite deposited sometime in the 1880s (Figure 14).

## 5.2 Turbidite Sediment Sources

To construct a reliable earthquake history and investigate what seismic parameters may be inferred from subaqueous evidence, an understanding of the physical properties and source area of the remobilized sediment is necessary. The sediment sources that compose climatically triggered turbidites have been widely studied in many depositional environments (i.e., sediment laden flood discharge) (e.g., Piper and Normark 2009; Talling, 2014; Wilhelm et al., 2015; 2017; Vandekerkhove et al., 2020), but sources of remobilized sediment during strong ground motion are not as well understood (Van Daele et al., 2015; Moernaut et al., 2014; Molenaar et al., 2021). This section focuses on identifying the sources of sediment incorporated in earthquake-related turbidites.

The deltaic slopes adjacent to the primary fluvial inputs appear to be the main sediment sources for the 2018 and 2016 earthquake turbidites, with some localized variability indicated in a few basins. In the basins where evidence of either earthquake is widespread, the turbidites increase in thickness and grain size towards the main deltaic environments (e.g., Figure 6a, 7, 11, 13, 15), in agreement with turbidity current evolution (Piper and Normark, 2009; Talling, 2014). In the basins with localized evidence, the deposits are observed at the base of slope adjacent to an auxiliary fan delta (Figure 9, 11b, 16). An exception is Passage Canal, where the 2018 turbidite (PC1) is observed to increase in thickness and grain size towards the Billings Creek fan, and not the primary fluvial input at the head of the fjord (Figure 15). However, this may be a result of the limited spatial distribution of cores in Passage Canal where the closest core to the fjord head delta is 6 km and not a result of lack of remobilization in that environment.

In Skilak Lake, there is evidence for remobilization of additional sediment sources beyond the main fluvial input (the Skilak River) during both earthquakes. Specifically, for events Sk1 and Sk2 in core SK20-02A, and Sk1 in core SK20-09A (Figure 5, 6a), which share characteristics with earthquake generated turbidites (i.e., bluish-grey basal color and inverse to normal grading) in co-located cores that are interpreted to be sourced from the remobilization of hemipelagic material (non-tributary source slope sediment) (Praet et al., 2022). Given the distance of cores SK20-02A and SK20-09A from the main fluvial sources (Figure 2), this unique sedimentological character is possibly the amalgamation of a local turbidite sourced from hemipelagic material (short runout distance and initial deposition) and the Skilak River delta sourced turbidite (longer runout distance and later deposition). Such an amalgamated turbidite has been observed in Chilean and Eklutna Lakes (Van Daele et al., 2017; 2020) and is further evidence of multiple synchronous slope failures within Skilak Lake.

The varied expressions of the 1964 earthquake suggest that different sedimentary environments were remobilized in different basins during that event. Acoustic profiles in Skilak and Kenai lakes show that the 1964 earthquake caused both delta and basin slopes to fail in large submarine landslides (MTDs) that subsequently evolved into megaturbidites (Figure 3, 4, and 8) (Praet et al., 2017). Similarly in Passage Canal, acoustic profiles and differential bathymetry provide evidence of a MTD and megaturbidite (Figure 15) sourced from failure of the main fjord head delta during the 1964 earthquake (Haeussler et al., 2014). In Tustumena Lake, although limited in coverage, the Chirp data and sediment cores show a large MTD (with blocky surface) and megaturbidite suggestive of a large subaqueous failure, likely of the main fluvial delta, during the 1964 earthquake (Figures 10 and 11). Compared to the Kenai Peninsula lakes (Kenai, Skilak, and Tustumena), the expression of the 1964 earthquake in Chelatna Lake is more subdued, with no evidence for an MTD or megaturbidite observed in Chirp data, but Chirp data do suggest that the main fluvial inputs are the source for remobilized sediment in 1964 (as well as during the 1991 and 2018 EQs) (Figure 14).

## 5.3 Minimum Shaking Intensity

The occurrence of two earthquakes closely spaced in time with similar magnitudes (i.e., the 2016 Iniskin and 2018 Anchorage earthquakes) allows us to investigate the Earthquake Recording Threshold (EQRT)—the minimum shaking intensity necessary to remobilize sediment—in southcentral Alaska. The proglacial lakes on the Kenai Peninsula (Kenai, Skilak, and Tustumena Lakes) are located adjacent to an axis connecting the two epicenters and are well situated to produce a tight constraint on the EQRT. Furthermore, the similarities in catchments and physiography for all the basins presented in this study (i.e., deep proglacial lakes or fjords) suggest that a direct comparison between historical earthquakes is possible and an apparent EQRT from one earthquake may apply to another in these basins (or similar basins elsewhere).

By observing the presence or absence of earthquake triggered turbidites, at varying distances from the 2018 and 2016 epicenters (48-142 km range), a gradient emerges in the volume of remobilized sediment and minimum shaking intensity required to trigger remobilization (Figure 17). Ground motions between MMI V-V1/2 appear sufficient to remobilize small amounts of sediment from some, but potentially not all deltaic slopes resulting in a highly localized deposit concentrated at the base of slope (e.g., Ke0, Tu0, and HF0). Once ground motions reach MMI V1/2 (+/-  $\sim 0.2$ ) enough material appears to be remobilized so that the deposit extends across the proximal basin with sufficient thickness that sedimentological properties may be utilized to potentially separate triggering mechanisms (e.g., Sk1, Tu1, Ch1, PC1). This finding differs from those of previous studies in which earthquake generated deposits, in non-proglacial lakes, were generated at shaking intensities near MMI V1/2 but confined to localized deltaic deposits (Moernaut et al., 2014). A noteworthy deviation is in the marine fjord environment of Passage Canal, where shaking intensities of MMI  $\sim$ V1/2 appear sufficient to have triggered sediment remobilization; but with the bulk of 2018 turbidite found in a small area adjacent to a deltaic slope (but still identifiable across the basin), it appears that a more limited quantity of sediment is remobilized in marine-deltaic environments at this shaking intensity, or that sediment gravity flow velocities decrease more rapidly in the glacial-marine environment.

The distribution and character of the 2018 and 2016 earthquake triggered deposits constrain how depositional environments respond to seismic shaking. Deltaic slopes appear to provide the main source of sediment for a majority of the turbidites triggered in 2016 and 2018, and with shaking intensities during those events not exceeding MMI VI (except at Eklutna Lake) it appears that similar to the subaqueous basins in Chile and the Swiss Alps (Monecke et al., 2004; Moernaut et al., 2014; Van Daele et al., 2015), the deltaic environments in southcentral Alaska are more susceptible to remobilization at a lower shaking intensity than basin slopes. This increase in sensitivity of deltaic slope is exemplified in Kenai Lake, where the  $\sim 0.5$  difference in shaking intensity between 2018 and 2016 was sufficient to overcome the EQRT in 2018 (MMI  $\sim$ V1/4), but not 2016 (MMI  $\sim$ IV3/4) (Figure 17b). This range for the generation of positive evidence (i.e., first appearance of localized slope failure) is slightly lower than what has been inferred in Chilean fjords (Vanneste et al., 2018). The threshold for the absence of negative evidence (i.e., shaking intensity above which a deposit will be observed) is also reasonably well constrained by the 2016 and 2018 deposits. For example, in Passage Canal a shaking intensity of MMI  $\sim$ V1/2 produced a deposit that was identifiable across the basin, whereas in nearby (and physiographically similar) Harriman Fjord the 2018 MMI of  $\sim$ V1/4 produced only localized deltaic failure. Tustumena Lake shows a similar relationship with a small, localized failure produced in 2018 (MMI  $\sim$ V) and a basin wide deposit produced in 2016 (MMI  $\sim$ V1/2-VI1/4). Higher shaking intensities during the  $M_w$  9.2 1964 Great Alaska earthquake caused earthquake generated deposits in all the basins surveyed (Figure 17b). In those lakes where a dense seismic grid provided sufficient coverage (i.e., Eklutna, Kenai, and Skilak), shaking intensity was high enough (MMI  $\sim$  VII1/4-VIII1/2) for failure to occur on both deltaic and basin slopes (Praet et al., 2017).

The nearly identical shaking intensities experienced at Skilak Lake during the 2016 and 2018 earthquakes is unique among the lakes surveyed and offers an opportunity to investigate potential variations in turbidite character in response to subtle changes in shaking intensity (Figure 2). The bluish-grey basal color and basal inverse grading in Sk1 and Sk2 (core SK20-02A) and Sk1 (core SK20-09A) provides evidence for sediment remobilization on basin slopes (non-tributary sourced), potentially at shaking intensities as low as MMI  $\sim$ V1/2. During the 2018 earthquake (Sk1) a majority of Skilak Lake experienced shaking intensity above MMI  $\sim$ V1/2 including along the slopes adjacent to SK20-09A (Figure 2). In contrast, in 2016 (Sk2) only

half of Skilak Lake appears to have experienced shaking intensities at or greater than  $\text{MMI} \sim V1/2$ , with slopes adjacent to SK20-09A experiencing less intense shaking than those located near SK20-02A (Figure 2). In core SK20-09A only the 2018 deposit contains evidence of remobilized sediment from the non-tributary source basin slope (Figure 5 and 6a). The lack of remobilized (non-deltaic) slope sediment in the 2016 deposit at SK20-09A, may therefore be related to the small eastward-directed decrease in shaking intensity across the lake basin during the 2016 earthquake. If true, this would imply that within the  $\sim 2$  km distance between SK20-02A and SK20-09A the shaking intensity dropped below the EQRT for non-deltaic slope sediment remobilization but did not drop below the EQRT for deltaic sediment as indicated by turbidite thickness and grain size distribution (Figure 6a and 7). In this discussion it is important to note that the MMI contours estimated by the USGS ShakeMap algorithm are not known to the precision of an individual coring location (Wald et al., 2012) and may not properly account for local site response, which may be considerable in lacustrine environments. An alternative explanation for the lack of slope sourced remobilized sediment in the 2016 deposit at SK20-09A, such as different flow pathways, cannot be ruled out with the current dataset.

The ShakeMap product for the 2018 Anchorage earthquake estimates an intensity of  $\text{MMI} < V$  at Chelatna Lake, but this may reflect the dearth of stations and *Did You Feel It?* (DYFI) reports within 50 km of the lake (USGS, 2018). Residents at Chelatna Lake during the 2018 Anchorage earthquake reported felt effects that indicate stronger shaking, including ‘violent shaking, swinging and falling objects, and thunderous noise of large wooden buildings shaking violently’ (M. Bertke, Chelatna Lake Lodge, written communication, 2021). These observations suggest a Community Decimal Intensity (analogous to MMI values) of about  $V1/2 (+/- 0.1)$  (Dengler and Dewey, 1998; Wald et al., 2012), a value that would bring the EQRT at Chelatna Lake in agreement with other lakes surveyed (Figure 17b). Moreover, the ground motion prediction equation (GMPE) used to calculate the ShakeMap ground motion values consistently underestimates the 2018 Anchorage earthquake at distances over 100 km (Figure 5 of West et al., 2020), and at a distance of  $\sim 140$  km the predicted Shakesmap MMI value for Chelatna Lake may reflect this underestimation. West et al. (2020) further comments that “a regionally tuned GMPE would likely bring this {GMPE underrepresentation at large distances} into better alignment”, which highlights an opportunity for lakes with well-calibrated EQRT to serve as potential remote site characterizations capable of recording a minimum shaking intensity to be a possible future input for GMPE products. The shaking experienced at Chelatna Lake during the  $M_w$  6.3 1991 intraslab earthquake (Ch2) was also potentially stronger than ShakeMap values suggest (i.e.,  $\text{MMI} IV1/2-V$ ), however due to the elapsed time since that event and residents moving from the area, direct answers to common DYFI questions are more difficult to ascertain (M. Bertke, Chelatna Lake Lodge, oral communication, 2021).

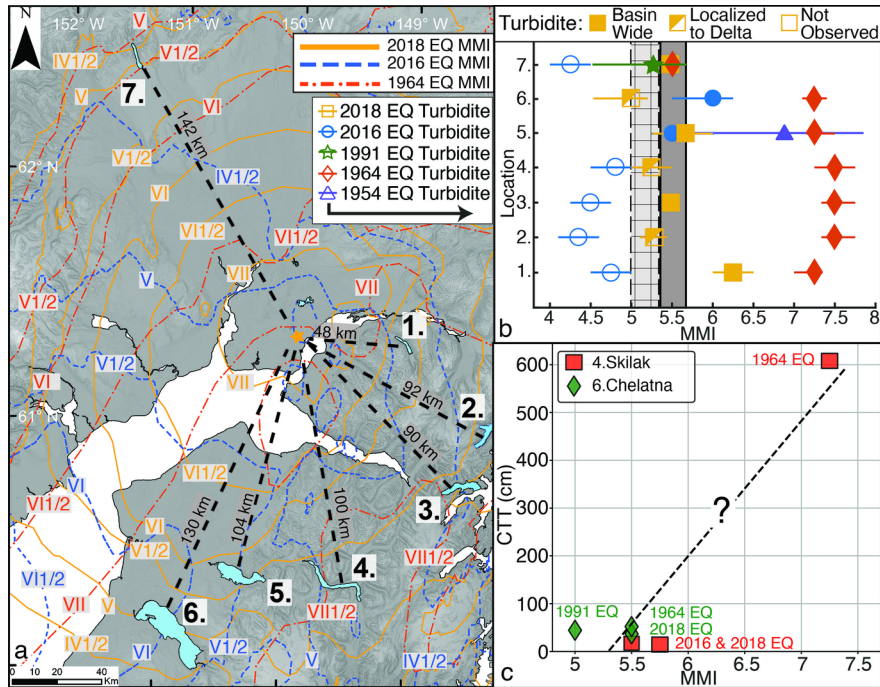


Figure 17: (a) ShakeMap derived MMI contours for the 2018, 2016, and 1964 earthquakes in the Upper Cook Inlet region (USGS 2016a; b; 2018). Study sites, plus Eklutna Lake (Van Daele et al., 2020), are labeled (1-7) with distances from the 2018 epicenter. 1. Eklutna Lake, 2. Harriman Fjord, 3. Passage Canal, 4. Kenai Lake, 5. Skilak Lake, 6. Tustumena Lake, 7. Chelatna Lake. (b) Estimated shaking intensity vs extent (or lack of) earthquake generated turbidite showing convergence on MMI V-V1/2 for the generation of highly localized deltaic deposit (grey hatched area), and MMI V1/2 for generation of a basin wide deposit with identifiable characteristics (dark grey). See text for discussion of estimated MMI at Chelatna Lake. (c) Cumulative Turbidite Thickness (CTT) vs Shaking Intensity for lakes with more than three observed earthquake generated deposits in a minimum of 10 cores.

In summary, an MMI of  $\sim$ V1/2 appears to represent the minimum shaking intensity required to remobilize enough sediment, primarily from deltaic slopes, to be identifiable (e.g.,  $> 5$  mm) so that an external trigger may be differentiated with methods employed in this study (Figure 17b). Sediment from non-tributary source slopes may be remobilized at this shaking intensity if those slopes experience elevated sedimentation rates and steep slope conditions. Deposits potentially triggered by shaking between MMI V-V1/2 are observed in a few cores, but are concentrated in highly localized areas near deltas (e.g., Ke0, Tu0, and HF0) (Figures 9, 11, and 16). However, in the absence of known historical events, these deposits lack the necessary thickness to be reliably identified and therefore may have limited usefulness as paleoseismic proxies, since distinguishing them from flood deposits (or background couplets) could prove difficult.

#### 5.4 Quantitative paleoseismology from subaqueous deposits in Alaska

The seismo-turbidites presented in this study are the result of three well-instrumented historical earthquakes and form a dataset that can be used to relate the seismic environment in southcentral Alaska to the regional subaqueous sedimentary response. The ability of lake deposits to reliably provide quantitative information on earthquake characteristics including recurrence interval, seismic sources, epicentral direction, and shaking intensity is an area of active research (e.g., Moernaut et al., 2014; Vanneste et al., 2018; Van Daele et al., 2019; 2020; Molenaar et al., 2021; Wils et al., 2021; Praet et al., 2022). An increasing amount of evidence is consistent with the remobilization of a thin veneer of surficial sediment providing the mechanism for

generation of a large number of seismo-turbidites (e.g., Moernaut et al., 2017; Molenaar et al., 2019; 2021). Furthermore, a correlative relationship between depth of remobilized sediment and seismic intensity suggest that quantitative seismic information may be determined from turbidite character (Moernaut et al., 2017; Molenaar et al., 2021).

A complete record of strong ground motions from subaqueous deposits requires that all earthquakes that exceed the EQRT generate a deposit regardless of interevent time or slope recharge conditions. The identification of two seismo-turbidites at Skilak Lake two years apart provides evidence that sufficient inter-event time (and by extension slope recharge time) is likely not a necessary condition for the generation of sediment remobilization by strong ground motion in proglacial Alaskan lakes, in agreement with previous studies in other high sedimentation settings (Moernaut et al., 2017; Wils et al., 2021). Furthermore, the ability to clearly distinguish two separate earthquakes so closely spaced in time is promising for the potential construction of long-term earthquake histories in southcentral Alaska.

Moernaut et al. (2014) suggests that the cumulative turbidite thickness (CTT) for an individual basin, calculated as the sum of individual deposit thicknesses across cores, correlates with seismic intensity. Although limited in the number of earthquake-generated deposits, the seismo-turbidites observed in Skilak Lake show a similar relationship (Figure 17c). The comparatively equal shaking intensities at Skilak Lake in 2018 and 2016 are reflected in similar CTT (13.76 and 16.51 cm, respectively), whereas the longer and more intense 1964 earthquake (~4 minutes, MMI >VIII/4; Plafker, 1969) resulted in a much larger CTT (604.95 cm). Moreover, in core SK20-02A, which is located near the intersection of the 2016 and 2018 MMI V1/2 contours (Figure 2), the thickness of the grey basal layer, indicative of non-deltaic slope sediment remobilization, is equally thick in the 2016 and 2018 deposit (Figure 6a) and is potential evidence that a similar depth of sediment was remobilized on the basin slopes during these two events. Although limited in the number of observations, the CTT of the 1954 deposit (25.13 cm) suggests that the proximity of that earthquake to Skilak Lake and the elevated shaking intensity (MMI ~VII1/2-VIII) (Doser, 2020), remobilized more sediment than the 2018 and 2016 earthquakes, despite the lower magnitude. Praet et al. (2022) attributes the difference in thickness between the 1954 and 1964 deposits, despite similar shaking intensities, to the longer duration and lower frequency component of the 1964 earthquake facilitating deeper remobilization.

The three earthquakes recorded at Chelatna Lake show a similar scaling of CTT with seismic intensity, however subtle differences are observed between the deposits that may be related to differences in individual earthquakes such as shaking duration or frequency content of ground motions. The 2018 and 1964 earthquakes caused similar intensities at Chelatna Lake (MMI ~V1/2) (Figure 17b), but the CTT of the 1964 deposit is thirty percent larger than the 2018 deposit (52.02 and 35.76 cm, respectively) (Figure 17c). The 1991 earthquake deposit CTT (38.32 cm) is similar to the 2018 deposit despite a lower shaking intensity (MMI ~V), however shaking during this event is not well constrained and may be higher. The differences between the deposits at Chelatna Lake may reflect the longer duration in 1964 allowing more oscillatory cycles to produce higher excess pore pressures that potentially remobilized a larger volume of sediment (Praet et al., 2022 and references therein).

In addition to cumulative turbidite thickness, the two types of seismically generated deposits identified (i.e., MTD with megaturbidites and thin turbidites) may reveal information about seismic sources. At the six basins located a similar distance (~250-280 km) inboard of the trench axis (basins 1-6, Figure 17), subaqueous landslides and megaturbidites are observed that record the 1964 earthquake (e.g., Figure 3, 8, 10, 15 and 16) (Haeussler et al., 2014; Praet et al., 2017; 2022). This may reflect the combination of high shaking intensities (MMI>VII) for long durations typical of megathrust earthquakes (Van Daele et al., 2019) that are sufficient to not only trigger surficial sediment remobilization, but also deep-seated slope failures that may develop into voluminous MTDs (Molenaar et al., 2021; Praet et al., 2022). At Chelatna Lake, about 500 km inboard of the trench axis, we observed no megaturbidites or subaqueous landslide deposits related to the 1964 earthquake (Figure 13), suggesting that the combination of lower shaking intensity and potential attenuation of the ground motion frequency spectrum did not elevate accumulated shear stress and excess pore pressure to a level sufficient to initiate failure on a deeper-seated failure plane (Praet et al.,

2022 and references therein). In contrast, intraslab earthquakes produce no observable evidence of MTDs or megaturbidites in all the surveyed basins, but instead are recorded by thin ( $< \sim 5$  cm) turbidites that likely result from remobilization and subsequent transport downslope of a thin veneer of surficial slope sediment (both deltaic and hemipelagic) (Moernaut et al., 2017; Molenaar et al., 2021; Praet et al., 2022).

In addition to the separation between intraslab versus megathrust events suggested by differences in the cumulative turbidite thickness and deposit character, basal grain size statistics may also reflect differences in seismic sources. The basal D80 and sorting values for the 2018, 2016, and 1964 deposits (primarily from Skilak Lake) suggest that close to deltaic slopes megathrust earthquakes are generally more poorly sorted energetic flows (Figure 6c), with the separation between seismic sources being more evident in basal D80 values away from fluvial sources (Figure A3). When normalized by deposit thickness, intraslab earthquakes plot higher on the basal D80/thickness ratio vs distance from fluvial source (Figure 6d). This relationship is more noticeable when the individual lake basins are examined separately. For example, grain size data from Eklutna (circles vs squares) and Skilak (diamonds/triangles vs stars) Lake turbidites record both intraslab and megathrust events (Figure 6c-e). Within each lake basin, a pattern emerges of higher basal D80/thickness values for intraslab earthquakes especially for deposits from the same core location (i.e., same distance from fluvial source, Figure 6d). Or, for a given basal D80, it appears that megathrust earthquakes tend to result in thicker deposits (Figure 6e), which may reflect potentially deeper-seated failure planes during megathrust events (Praet et al., 2022).

An area of active research is the potential ability to extract epicentral directionality information from lacustrine sediments (e.g., Howarth et al., 2014; Vanneste et al., 2018; Van Daele et al., 2020). By assuming that factors related to turbidite initiation and flow conditions such as slope angle, basin physiography, and sedimentological character do not change substantially between successive strong ground motion events (i.e., constant local site effects), a direct comparison of deposits at individual coring locations may yield information about variations in local shaking intensity (Van Daele et al., 2020). Using this reasoning at Eklutna Lake, Van Daele et al. (2020) inferred that the anomalously high ratio of 2018:1964 turbidite thickness in the direction of the 2018 epicenter provides evidence of a gradient in strong ground motion that is reflected in the relative turbidite thickness.

Although the longitudinal axis of Eklutna Lake is better aligned toward the 2018 epicenter than Skilak Lake, whose longitudinal axis orientation is more perpendicular, a similar exercise yields similar results (Figure 7). In Skilak Lake, turbidite thickness ratios of both the 2018:1964 and the 2016:1964 deposits increase towards the distal sub-basin and the direction of increasing strong ground motion (Figure 2 and 7), indicating that relative turbidite thicknesses in Skilak Lake may also be sensitive to epicenter location. Skilak Lake experienced uniform shaking intensity (MMI VIII $\frac{1}{2}$ ) in 1964. It is unclear what effect the very large thickness of the Skilak Lake 1964 megaturbidite in the proximal basin, or the lack of defined varve and deposit boundaries in the distal basin, may have on this ratio. Although further investigations on additional lake basins would further test this hypothesis, the ability to determine epicentral direction from lacustrine sediments could provide a valuable tool in the construction of long earthquake records from multiple lakes.

## 6. Conclusion

Seven subaqueous basins in southcentral Alaska are investigated for a record of the Mw 7.1 2018 Anchorage, Mw 7.1 2016 Iniskin, and Mw 9.2 1964 Great Alaska earthquakes through a variety of gravity driven sediment flows (MTD, megaturbidites, and turbidites). Sedimentological characteristics of the resulting earthquake generated deposit are distinctly different from those with a climatic origin. The spatial occurrence of seismo-turbidites from the 2016 and 2018 earthquakes constrain the subaqueous EQRT for southcentral Alaska to MMI  $\sim$ V-V $\frac{1}{2}$ . At MMI  $\sim$ V $\frac{1}{2}$ , deltaic slopes appear to be the main source of remobilized sediment during these events, with minor amounts of non-tributary sourced sediment potentially remobilized in high sedimentation areas with steep slopes. Turbidites generated by shaking during intraslab events (i.e., 2018 and 2016 earthquakes) are thin ( $< \sim 5$  cm), light-colored, coarse-grained normally graded deposits. The deposits generated by ground motions during megathrust events (i.e., the 1964 earthquake) share these sedimentological characteristics, but tend to be more voluminous and are often associated with MTDs and

megaturbidites in acoustic data, especially near the megathrust rupture area. Separation of seismic source appears to be possible through a comparison of basal grain size statistic and deposit thickness revealing that megathrust events appear to generate thicker, more voluminous, faster flows. A further comparison of deposit thickness within the same basin reveals that relative thickness of seismo-turbidites may be sensitive to gradients in strong ground motion, possibly revealing information on epicenter directionality.

## 7. Acknowledgements

We thank Nore Praet and Maarten Van Daele for early discussions on lacustrine targets in southcentral Alaska; we thank Thomas Lorenson for his assistance in the dating of radioisotopes; we also thank Sylvia Nicovich, Katleen Wils, and Maarten Van Daele for their reviews and comments that greatly improved the quality of this manuscript. Any use of trade, firm, or product names is for descriptive purposes only and does not imply endorsement by the U.S. Government.

## 8. Availability Statement

The Chirp acoustic data used in this study to interpret the sub-surface geology are available through <https://doi.org/10.5066/P924775B> (Singleton et al., 2023). The core data including, high-resolution photography, orthogonal CT slices, MSCL data, and raw grain size measurements, used to interpret the lacustrine stratigraphy and sedimentology are available through <https://doi.org/10.5066/P924775B> (Singleton et al., 2023).

## 9. References

- Alaska Division of Fish and Game (ADF&G). (2015). Alaska Lake Database, [http://www.adfg.alaska.gov/SF\\_Lakes/](http://www.adfg.alaska.gov/SF_Lakes/) (last accessed March, 2022).
- Altamimi, Z., Reischung, P., Métivier, L., & Collilieux, X. (2016). ITRF2014: A new release of the International Terrestrial Reference Frame modeling nonlinear station motions. *Journal of geophysical research: solid earth* , 121 (8), 6109-6131.
- Avşar, U., Jónsson, S., Avşar, Ö., & Schmidt, S. (2016). Earthquake-induced soft-sediment deformations and seismically amplified erosion rates recorded in varved sediments of Koyceğiz Lake (SW Turkey). *Journal of Geophysical Research: Solid Earth* , 121 (6), 4767-4779.
- Avşar, U., Hubert-Ferrari, A., De Batist, M., Lepoint, G., Schmidt, S., & Fagel, N. (2014). Seismically-triggered organic-rich layers in recent sediments from Göllüköy Lake (North Anatolian Fault, Turkey). *Quaternary Science Reviews* , 103 , 67-80.
- Avşar, U., Hubert-Ferrari, A., Batist, M. D., & Fagel, N. (2014). A 3400 year lacustrine paleoseismic record from the North Anatolian Fault, Turkey: Implications for bimodal recurrence behavior. *Geophysical Research Letters* , 41 (2), 377-384.
- Beck, C. (2009). Late Quaternary lacustrine paleo-seismic archives in north-western Alps: Examples of earthquake-origin assessment of sedimentary disturbances. *Earth-Science Reviews* , 96 (4), 327-344.
- Beck, S., Barrientos, S., Kausel, E., & Reyes, M. (1998). Source characteristics of historic earthquakes along the central Chile subduction Askew et Alzone. *Journal of South American Earth Sciences* , 11 (2), 115-129.
- Bertke, M. (2021). Chelatna Lake Lodge owner and year-round resident at Chelatna Lake – experienced the 2018 Anchorage Earthquake at Chelatna Lake. (<https://www.chelatna.com>) *written and oral communication June, 2021*.
- Brothers, D. S., Haeussler, P. J., Liberty, L., Finlayson, D., Geist, E., Labay, K., & Byerly, M. (2016). A submarine landslide source for the devastating 1964 Chenega tsunami, southern Alaska. *Earth and Planetary Science Letters* , 438 , 112-121.
- Boes, E., Van Daele, M., Moernaut, J., Schmidt, S., Jensen, B. J., Praet, N., . . . & De Batist, M. (2018). Varve formation during the past three centuries in three large proglacial lakes in south-central Alaska. *GSA*

*Bulletin* , 130 (5-6), 757-774.

Bouma, A. H. (1987). Megaturbidite: an acceptable term?. *Geo-Marine Letters* , 7 (2), 63-67.

Chang, S. E., & Falit-Baiamonte, A. (2002). Disaster vulnerability of businesses in the 2001 Nisqually earthquake. *Global Environmental Change Part B: Environmental Hazards* , 4 (2), 59-71.

Dengler, L. A., & Dewey, J. W. (1998). An intensity survey of households affected by the Northridge, California, earthquake of 17 January 1994. *Bulletin of the Seismological Society of America* , 88 (2), 441-462.

Dernie, K. M., Kaiser, M. J., & Warwick, R. M. (2003). Recovery rates of benthic communities following physical disturbance. *Journal of animal ecology* , 72 (6), 1043-1056.

Doser, D. I. (2020). Analysis of intraslab predigital earthquakes of the south-central Alaska region. *Seismological Research Letters* , 91 (3), 1367-1376.

Frankel, A., Chen, R., Petersen, M., Moschetti, M., & Sherrod, B. (2015). 2014 update of the Pacific Northwest portion of the US National Seismic Hazard Maps. *Earthquake Spectra* , 31 (1\_suppl), S131-S148.

Froján, C. R. B., Cooper, K. M., Bremner, J., Defew, E. C., Hussin, W. M. W., & Paterson, D. M. (2011). Assessing the recovery of functional diversity after sustained sediment screening at an aggregate dredging site in the North Sea. *Estuarine, Coastal and Shelf Science* , 92 (3), 358-366.

Goldfinger, C., Nelson, C. H., Morey, A. E., Johnson, J. E., Patton, J. R., Karabanov, E. B., ... & Vallier, T. (2012). *Turbidite event history—Methods and implications for Holocene paleoseismicity of the Cascadia subduction zone* (No. 1661-F). US Geological Survey.

Haeussler, P. J., Parsons, T., Finlayson, D. P., Hart, P., Chaytor, J. D., Ryan, H., ... & Liberty, L. (2014). New imaging of submarine landslides from the 1964 earthquake near Whittier, Alaska, and a comparison to failures in other Alaskan fjords. In *Submarine mass movements and their consequences* (pp. 361-370). Springer, Cham.

Haeussler, P. J., Saltus, R. W., Stanley, R. G., Ruppert, N., Lewis, K., Karl, S. M., & Bender, A. (2017). The Peters Hills basin, a Neogene wedge-top basin on the Broad Pass thrust fault, south-central Alaska. *Geosphere* , 13 (5), 1464-1488.

Heifetz, E., Agnon, A., & Marco, S. (2005). Soft sediment deformation by Kelvin Helmholtz Instability: A case from Dead Sea earthquakes. *Earth and Planetary Science Letters* , 236 (1-2), 497-504.

Howarth, J. D., Fitzsimons, S. J., Norris, R. J., & Jacobsen, G. E. (2014). Lake sediments record high intensity shaking that provides insight into the location and rupture length of large earthquakes on the Alpine Fault, New Zealand. *Earth and Planetary Science Letters* , 403 , 340-351.

Jibson, R. W., Grant, A. R., Witter, R. C., Allstadt, K. E., Thompson, E. M., & Bender, A. M. (2020). Ground failure from the Anchorage, Alaska, earthquake of 30 November 2018. *Seismological Research Letters* , 91 (1), 19-32.

Mann, M. E., & Abers, G. A. (2020). First-order mantle subduction-zone structure effects on ground motion: The 2016 Mw 7.1 Iniskin and 2018 Mw 7.1 Anchorage earthquakes. *Seismological Research Letters* , 91 (1), 85-93.

McCulloch, D. S. (1966). Slide-induced waves, seiching, and ground fracturing caused by the earthquake of March 27, 1964, at Kenai Lake, Alaska.

Moernaut, J., Daele, M. V., Heirman, K., Fontijn, K., Strasser, M., Pino, M., ... & De Batist, M. (2014). Lacustrine turbidites as a tool for quantitative earthquake reconstruction: New evidence for a variable rupture mode in south central Chile. *Journal of Geophysical Research: Solid Earth* , 119 (3), 1607-1633.

- Moernaut, J., Van Daele, M., Strasser, M., Clare, M.A., Heirman, K., Viel, M., Cardenas, J., Kilian, R., de Guevara, B.L., Pino, M. and Urrutia, R., 2017. Lacustrine turbidites produced by surficial slope sediment remobilization: a mechanism for continuous and sensitive turbidite paleoseismic records. *Marine Geology* , 384 , 159-176.
- Moernaut, J., Van Daele, M., Strasser, M., Clare, M. A., Heirman, K., Viel, M., ... & De Batist, M. (2017). Lacustrine turbidites produced by surficial slope sediment remobilization: a mechanism for continuous and sensitive turbidite paleoseismic records. *Marine Geology* , 384 , 159-176.
- Molenaar, A., Van Daele, M., Vandorpe, T., Degenhart, G., De Batist, M., Urrutia, R., ... & Moernaut, J. (2021). What controls the remobilization and deformation of surficial sediment by seismic shaking? Linking lacustrine slope stratigraphy to great earthquakes in South–Central Chile. *Sedimentology* , 68 (6), 2365-2396.
- Molenaar, A., Van Daele, M., Huang, J.-J. S., Strasser, M., De Batist, M., Pino, M., Urrutia, R. and Moernaut, J. (2022). "Disentangling factors controlling earthquake-triggered soft-sediment deformation in lakes." *Sedimentary Geology* 438 .
- Monecke, K., Anselmetti, F. S., Becker, A., Sturm, M., & Giardini, D. (2004). The record of historic earthquakes in lake sediments of Central Switzerland. *Tectonophysics* , 394 (1-2), 21-40.
- Mulliken, K. M., Schaefer, J., & Cameron, C. E. (2018). *Geospatial Distribution of Tephra Fall in Alaska: A Geodatabase Compilation of Published Tephra Fall Occurrences from the Pleistocene to the Present* . State of Alaska, Department of Natural Resources, Division of Geological & Geophysical Surveys.
- Oguri, K., Kawamura, K., Sakaguchi, A., Toyofuku, T., Kasaya, T., Murayama, M., ... & Kitazato, H. (2013). Hadal disturbance in the Japan Trench induced by the 2011 Tohoku–Oki Earthquake. *Scientific Reports* , 3 (1), 1-6.
- Patton, J. R., Goldfinger, C., Morey, A. E., Romsos, C., Black, B., & Djadjadihardja, Y. (2013). Seismoturbidite record as preserved at core sites at the Cascadia and Sumatra–Andaman subduction zones. *Natural Hazards and Earth System Sciences* , 13 (4), 833-867.
- Pennington, W., Tutin, T. G., Cambray, R. S., & Fisher, E. M. (1973). Observations on lake sediments using fallout <sup>137</sup>Cs as a tracer. *Nature* , 242 (5396), 324-326.
- Plafker, G. (1969). Tectonics of the March 27, 1964 Alaska earthquake.
- Plafker, G., Kachadoorian, R., Eckel, E. B., & Mayo, L. R. (1969). *Effects of the earthquake of March 27, 1964 on various communities* (pp. 1-50). US Government Printing Office.
- Piper, D. J., & Normark, W. R. (2009). Processes that initiate turbidity currents and their influence on turbidites: a marine geology perspective. *Journal of Sedimentary Research* , 79 (6), 347-362.
- Praet, N., Moernaut, J., Van Daele, M., Boes, E., Haeussler, P. J., Strupler, M., ... & De Batist, M. (2017). Paleoseismic potential of sublacustrine landslide records in a high-seismicity setting (south-central Alaska). *Marine Geology* , 384 , 103-119.
- Praet, N., Van Daele, M., Moernaut, J., Mestdagh, T., Vandorpe, T., Jensen, B. J., ... & De Batist, M. (2022). Unravelling a 2300 year long sedimentary record of megathrust and intraslab earthquakes in proglacial Skilak Lake, south-central Alaska. *Sedimentology* .
- Roland, E., Haeussler, P., Parsons, T., & Hart, P. (2020). Submarine landslide kinematics derived from high-resolution imaging in Port Valdez, Alaska. *Journal of Geophysical Research: Solid Earth* , 125 (7), e2019JB018007.
- Sahakian, V. J., Melgar, D., Quintanar, L., Ramirez-Guzman, L., Perez-Campos, X., & Baltay, A. (2018). Ground motions from the 7 and 19 September 2017 Tehuantepec and Puebla-Morelos, Mexico, earthquakes. *Bulletin of the Seismological Society of America* , 108 (6), 3300-3312. doi: 10.1785/0120180108.

- Schnellmann, M., Anselmetti, F. S., Giardini, D., McKenzie, J. A., & Ward, S. N. (2002). Prehistoric earthquake history revealed by lacustrine slump deposits. *Geology*, *30* (12), 1131-1134.
- Schneider, C. A., Rasband, W. S., & Eliceiri, K. W. (2012). NIH Image to ImageJ: 25 years of image analysis. *Nature methods*, *9* (7), 671-675.
- Singleton, D.M., Brothers, D.S., Hill, J.C., Haeussler, P.J., and Witter, R.C., 2023, Geophysical and core sample data collected in lakes and fjords of southcentral Alaska following the 2018 Anchorage earthquake: *U.S. Geological Survey data release*, <https://doi.org/10.5066/P924775B>.
- Strasser, M., Anselmetti, F. S., Fah, D., Giardini, D., & Schnellmann, M. (2006). Magnitudes and source areas of large prehistoric northern Alpine earthquakes revealed by slope failures in lakes. *Geology*, *34* (12), 1005-1008.
- Talling, P. J. (2014). On the triggers, resulting flow types and frequencies of subaqueous sediment density flows in different settings. *Marine Geology*, *352*, 155-182.
- U.S. Geological Survey (USGS). (2016a). Earthquake Hazards Program: M 7.1 – 47 km ESE of Pedro Bay, Alaska, <https://earthquake.usgs.gov/earthquakes/eventpage/ak01613v15nv/executive> (last accessed March, 2022).
- U.S. Geological Survey (USGS). (2016b). Earthquake Hazards Program: M 9.2 Alaska Earthquake and Tsunami of March 27, 1964, <https://earthquake.usgs.gov/earthquakes/events/alaska1964/> (last accessed March, 2022).
- U.S. Geological Survey (USGS). (2016c). Earthquake Hazards Program: M 6.3 – Central Alaska, <https://earthquake.usgs.gov/earthquakes/eventpage/ak9915k8az9c/executive> (last accessed August, 2022).
- U.S. Geological Survey (USGS). (2018). Earthquake Hazards Program: M 7.1 - 14km NNW of Anchorage, Alaska, <https://earthquake.usgs.gov/earthquakes/eventpage/ak20419010/executive> (last accessed March, 2022).
- U.S. Geological Survey (USGS). (2020) Quaternary Fault and Fold Database for the Nation, last accessed August, 2022, at <https://doi.org/10.5066/P9BCVRCK>.
- U.S. Geological Survey (USGS). (2021). USGS water data for the Nation: U.S. Geological Survey National Water Information System database, <http://dx.doi.org/10.5066/F7P55KJN> (last accessed February 9, 2021).
- Van Daele, M., Moernaut, J., Doom, L., Boes, E., Fontijn, K., Heirman, K., ... & De Batist, M. (2015). A comparison of the sedimentary records of the 1960 and 2010 great Chilean earthquakes in 17 lakes: Implications for quantitative lacustrine palaeoseismology. *Sedimentology*, *62* (5), 1466-1496.
- Van Daele, M., Meyer, I., Moernaut, J., De Decker, S., Verschuren, D., & De Batist, M. (2017). A revised classification and terminology for stacked and amalgamated turbidites in environments dominated by (hemi) pelagic sedimentation. *Sedimentary Geology*, *357*, 72-82.
- Van Daele, M., Araya-Cornejo, C., Pille, T., Vanneste, K., Moernaut, J., Schmidt, S., ... & Cisternas, M. (2019). Distinguishing intraplate from megathrust earthquakes using lacustrine turbidites. *Geology*, *47* (2), 127-130.
- Van Daele, M., Haeussler, P. J., Witter, R. C., Praet, N., & De Batist, M. (2020). The sedimentary record of the 2018 Anchorage earthquake in Eklutna Lake, Alaska: Calibrating the lacustrine seismograph. *Seismological Research Letters*, *91* (1), 126-141.
- Vandekerckhove, E., Van Daele, M., Praet, N., Cnudde, V., Haeussler, P. J., & De Batist, M. (2020). Flood-triggered versus earthquake-triggered turbidites: A sedimentological study in clastic lake sediments (Eklutna Lake, Alaska). *Sedimentology*, *67* (1), 364-389.

Vanneste, K., Wils, K. and Van Daele, M. (2018). "Probabilistic Evaluation of Fault Sources Based on Paleoseismic Evidence From Mass-Transport Deposits: The Example of Aysén Fjord, Chile." *Journal of Geophysical Research: Solid Earth* 123(11): 9842-9865.

Wald, D. J., Quitoriano, V., Worden, C. B., Hopper, M., & Dewey, J. W. (2011). USGS "Did You Feel It?" internet-based macroseismic intensity maps. *Annals of geophysics* , 54 (6).

Waye-Barker, G. A., McIlwaine, P., Lozach, S., & Cooper, K. M. (2015). The effects of marine sand and gravel extraction on the sediment composition and macrofaunal community of a commercial dredging site (15 years post-dredging). *Marine Pollution Bulletin* , 99 (1-2), 207-215.

West, M. E., Bender, A., Gardine, M., Gardine, L., Gately, K., Haeussler, P., ... & Witter, R. (2020). The 30 november 2018 Mw 7.1 anchorage earthquake. *Seismological Research Letters* , 91 (1), 66-84.

Wilhelm, B., Sabatier, P., & Arnaud, F. (2015). Is a regional flood signal reproducible from lake sediments?. *Sedimentology* , 62 (4), 1103-1117.

Wilhelm, B., Vogel, H., & Anselmetti, F. S. (2017). A multi-centennial record of past floods and earthquakes in Valle d'Aosta, Mediterranean Italian Alps. *Natural Hazards and Earth System Sciences* , 17 (5), 613-625.

Wils, K., Deprez, M., Kissel, C., Vervoort, M., Van Daele, M., Daryono, M. R., ... & De Batist, M. (2021). Earthquake doublet revealed by multiple pulses in lacustrine seismo-turbidites. *Geology* , 49 (11), 1301-1306.

Zolitschka, B., Francus, P., Ojala, A. E., & Schimmelmann, A. (2015). Varves in lake sediments—a review. *Quaternary Science Reviews* , 117 , 1-41.

## Appendix A:

The figures and tables in this appendix contain contributing information to the publication "Constraining the earthquake recording threshold of intraslab earthquakes with turbidites in southcentral Alaska's lakes and fjords" by Singleton et al., presented in *Tectonics of Alaska and Western Canada*. The information in the figures and tables below concern basic background sedimentological data related to seismically (and climatically) triggered turbidites in lakes and fjords of southcentral Alaska. All grain size data presented below is available through Singleton et al. (2023).

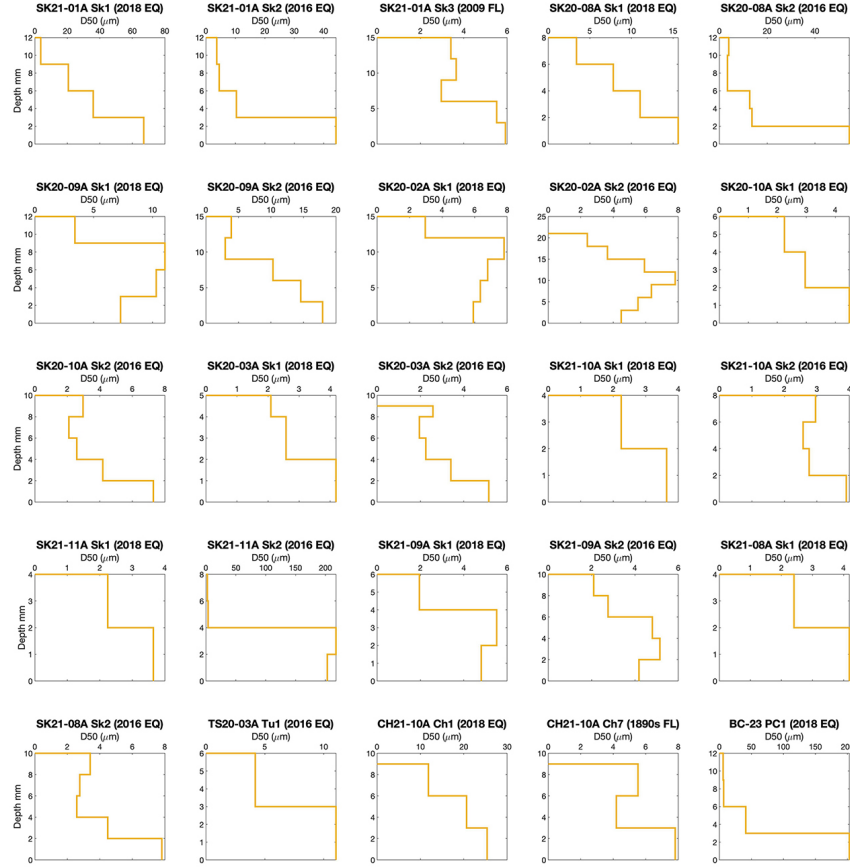


**Figure A1.** Grain size D50 values of select event deposits from all the surveyed basins. Depth relative to turbidite base (base @ 0 mm). Grain size data available in Singleton et al., (2023).

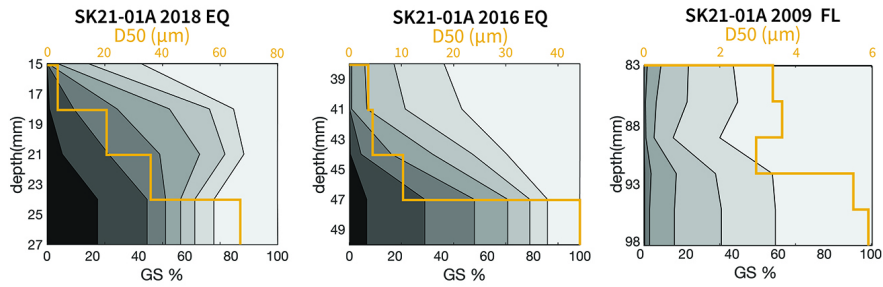


**Figure A2.** Grain size distribution for climatic vs seismic event deposits in SK21-01A. Grain size data available in Singleton et al. (2023).

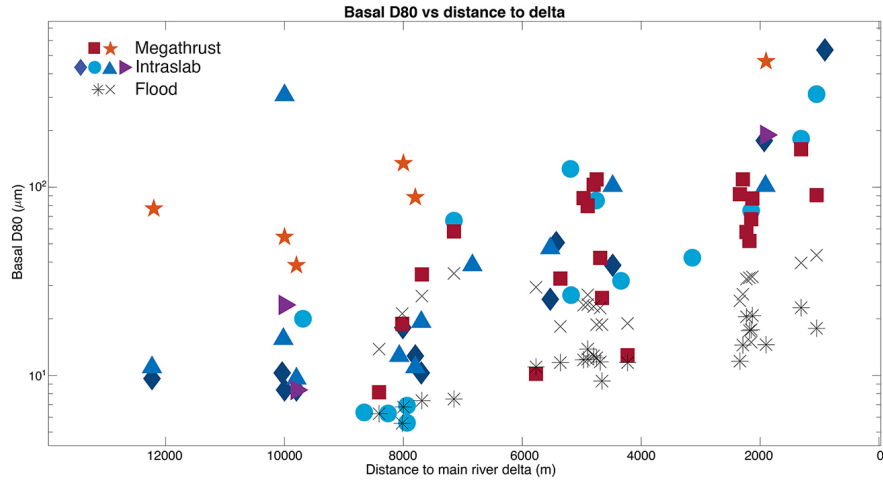


**Figure A3.** Basal D80 values vs distance to main fluvial input for select cores in all surveyed basins. General pattern of separation between seismic source (i.e., megathrust vs intraslab) is observed, especially in cores located away from fluvial source. Symbols and references are the same as Figure 6c-e. Grain size data available in Singleton et al. (2023).

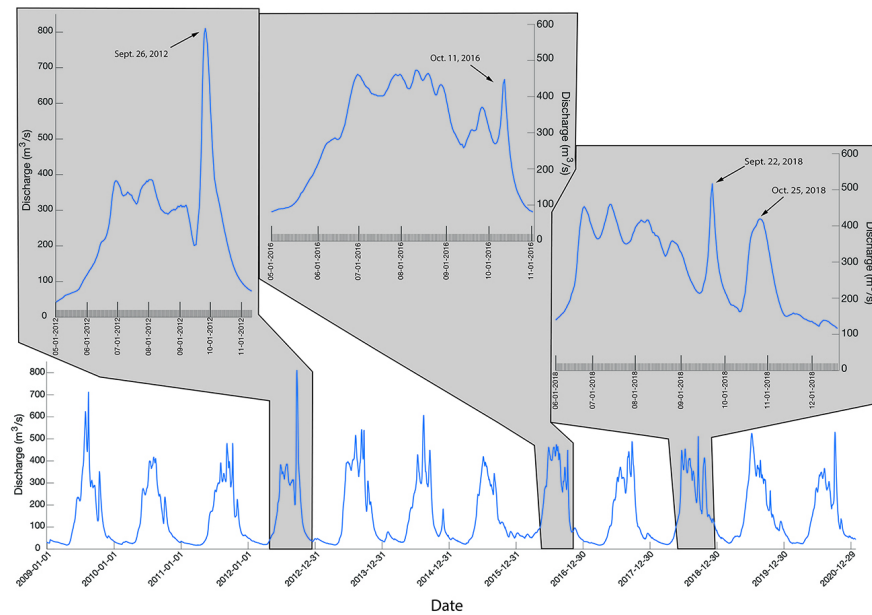


**Figure A4: Kenai River – Skilak Outlet Climate signal**

Mean daily discharge on the Kenai River at the Skilak Lake outlet (Gauge Number USGS 15266110). See Figure 2 for location of Station (black square). Data taken from USGS, (2021).

**Table A1. Skilak Lake Turbidite Thickness and Grain Size**

**Hosted file**

image22.emf available at <https://authorea.com/users/695394/articles/684128-constraining-the-earthquake-recording-threshold-of-intraslab-earthquakes-with-turbidites-in-southcentral->

[alaska-s-lakes-and-fjords](#)

Note. CTT = Cumulative Turbidite Thickness. Data available in Singleton et al. (2023).

**Table A1 Continued. *Skilak Lake Turbidite Thickness and Grain Size***

**Hosted file**

image23.emf available at <https://authorea.com/users/695394/articles/684128-constraining-the-earthquake-recording-threshold-of-intraslab-earthquakes-with-turbidites-in-southcentral-alaska-s-lakes-and-fjords>

Note. CTT = Cumulative Turbidite Thickness. Data available in Singleton et al. (2023).

**Table A2. *Chelatna Lake Turbidite Thickness and Grain Size***

**Hosted file**

image24.emf available at <https://authorea.com/users/695394/articles/684128-constraining-the-earthquake-recording-threshold-of-intraslab-earthquakes-with-turbidites-in-southcentral-alaska-s-lakes-and-fjords>

Note. CTT = Cumulative Turbidite Thickness. Data available in Singleton et al. (2023).

**Table A3. *Tustumena Lake Turbidite Thickness and Grain Size***

**Hosted file**

image25.emf available at <https://authorea.com/users/695394/articles/684128-constraining-the-earthquake-recording-threshold-of-intraslab-earthquakes-with-turbidites-in-southcentral-alaska-s-lakes-and-fjords>

Note. CTT = Cumulative Turbidite Thickness. Data available in Singleton et al. (2023).

**Table A4. *Passage Canal and Harriman Fjord Turbidite Thickness and Grain Size***

**Hosted file**

image26.emf available at <https://authorea.com/users/695394/articles/684128-constraining-the-earthquake-recording-threshold-of-intraslab-earthquakes-with-turbidites-in-southcentral-alaska-s-lakes-and-fjords>

Note. CTT = Cumulative Turbidite Thickness. Data available in Singleton et al. (2023).

**Table A5. *Kenai Lake Turbidite Thickness and Grain Size***

**Hosted file**

image27.emf available at <https://authorea.com/users/695394/articles/684128-constraining-the-earthquake-recording-threshold-of-intraslab-earthquakes-with-turbidites-in-southcentral-alaska-s-lakes-and-fjords>

Note. CTT = Cumulative Turbidite Thickness. Data available in Singleton et al. (2023).